

Final Report

**Effects of Within-Day and Within-Week Peaking on Bank
Erosion at the Roanoke River Downstream of the Roanoke
Rapids Dam**

**John Petrie
Soonkie Nam
Panayiotis Diplas
Marte S. Gutierrez**

December 22, 2010

**Sponsors:
Dominion
United States Army Corps of Engineer**

Table of Contents

Executive Summary	iv
1. Introduction.....	1
2. Fluvial Erosion of Cohesive Riverbanks	4
2.1 Overview of the Jet Test	5
2.2 Discussion of Results.....	7
3. Soil Permeability.....	11
4. Computational Fluid Dynamics	20
4.1 Straight Reach.....	20
4.2 Meander Bend.....	24
5. Geotechnical Modeling.....	30
5.1 Fluvial Erosion.....	31
5.2 Small Scale Failures.....	35
6. Overbank Flows	37
7. Results.....	43
7.1 Fluvial Erosion.....	43
7.2 Slope Stability.....	45
7.3 Small Scale Failures.....	46
7.5 Coupled Stability Analysis	51
8. Conclusions.....	54
9. References	56
10. Appendices.....	61

List of Figures

Figure 1.1. Map of the study reach.	1
Figure 2.1. Diagram of jet, scour, and relative shear stress distribution.	5
Figure 2.2. Jet test apparatus installed at Site 1 during testing in May, 2010.	6
Figure 2.3. Critical shear stress and erodibility coefficient.	9
Figure 3.1. Schematic of the auger hole method.	13
Figure 3.2. Guelph permeameter testing device installed on the lower Roanoke River.	14
Figure 3.3. GWT modeling at Site 1.	15
Figure 3.4. Cracks, pores and proof of structured soils after jet test.	16
Figure 3.5. Location of USGS GWT measurement data.	17
Figure 3.6. Variation of GWT and WSE.	18

Figure 4.1. Domain and boundaries for Site 5 CFD simulations.....	21
Figure 4.2. Numerical mesh at the left bank of Site 5 CFD simulations.	22
Figure 4.3. Boundary shear stress distribution at Site 5.	23
Figure 4.4. Contours of velocity magnitude at Site 5.	23
Figure 4.5. Water surface geometry for CFD model of Site 1.....	24
Figure 4.6. Channel geometry at Site 1.....	25
Figure 4.7. Example of the numerical mesh within the channel bend.....	25
Figure 4.8. Contour plot of water surface velocity magnitude at Site 1.	27
Figure 4.9. Contour plot of boundary shear stress at Site 1.....	27
Figure 4.10. Boundary shear stress at the bend apex.....	28
Figure 4.11. Distribution of boundary shear stress near the erosion pins at Site 1.....	28
Figure 4.12. Contour plots of velocity magnitude near the erosion pins at Site 1	29
Figure 5.1. Flowchart illustrating the procedure for the slope stability analysis.	32
Figure 5.2. Cumulative erosion based on the erosion pin data.	33
Figure 5.3. Small scale failures on the lower Roanoke River.....	35
Figure 5.4. Schematic view of small scale failures.....	36
Figure 6.1. Summary of overbank hydraulics.....	37
Figure 6.2. Modeling of flood flow condition.	40
Figure 6.3. WSE changes at Site 1.....	41
Figure 6.4. Step-down flow rate and WSE at Site 1.	42
Figure 7.1 Estimated erosion of the left bank at Site 1.....	44
Figure 7.2. Example of overbank flow conditions at Site 4.....	45
Figure 7.3. Example of a small scale failure with tension cracks near the WSE at Site 1.	47
Figure 7.4. Changes in factor of safety over time during a rapid drawdown event.....	48
Figure 7.5. Factor of safety at each site for step-down flow conditions.....	49
Figure 7.6 Factor of safety with lower permeability for step-down flow scenario.....	50
Figure 7.7. Unstable slope after step-down with lower permeability.	50
Figure 7.8. Prediction of profile changes due to fluvial erosion over ten years at Site 1.	52
Figure 7.9. Prediction of profile changes due to fluvial erosion over ten years at Site 2.	52

List of Tables

Table 2.1. Descriptive Statistics for k_d and τ_c	8
Table 2.2. Sample size by site and soil type	10
Table 3.1. Average values of permeability from different methods	15
Table 3.2. Locations of far left boundary condition and WSE	19
Table 6.1. Water surface elevations during flood flow condition	40
Table 6.2. Extended results of slope stability modeling (steady state)	40
Table 7.1. Factor of safety at each site for steady state flow conditions	45
Table 7.2. Factor of safety changes after ten years of erosion.....	53

Executive Summary

This report serves to summarize the work that has been completed on erosion and stability since the last report was submitted in December 2009. The work carried out for this report includes additional field work to characterize the permeability and erodibility of the bank soils, improved numerical simulations of river flow and bank stability, as well as analyses of step-down scenarios and overbank flows. About one week was spent in the field performing additional jet tests for erodibility and several different in situ permeability tests in an effort to improve the estimates of various important soil parameters/properties. Further permeability tests were completed in the laboratory. Access to a new preprocessing program, ICEM-CFD, allowed improved numerical meshes to be generated for the computational fluid dynamics (CFD) analysis. The results of these simulations provide a more accurate and detailed picture of the flow processes on the lower Roanoke River and how they affect fluvial erosion. Slope stability modeling was extended to include all five study sites under steady state and transient flow conditions. The slope stability analysis also benefited from the detailed investigation into the permeability of the riverbank soil.

These refinements in modeling were used to assess the impacts of different flow releases on fluvial erosion and bank stability. Among the scenarios, two new cases were also considered in detail; that of the step-down in flow rate following flood control flow releases and an increase in the flood control flow rate. The current flood control flow rate of about $565 \text{ m}^3/\text{s}$ (20,000 cfs) results in bankfull conditions along the study reach. Thus, an increase in this flow rate will result in overbank flow, where the river water spills onto the floodplain introducing additional complexities to the dynamic behavior of the flow. A simplified approach is used to estimate the effects of increasing the flood control flow releases from $565 \text{ m}^3/\text{s}$ (20,000 cfs) to $990 \text{ m}^3/\text{s}$ (35,000 cfs) on riverbank stability.

While details of each analysis are provided in the report text, a summary of the important conclusions is provided below. Further discussion of each topic can be found in the final chapter of this report.

1. The types of cohesive soils in the riverbank have similar engineering properties but exhibit a wide range of erodibility parameters. This finding is not uncommon and is supported by the significant variability in the erosion pin data at various sites (Schenk et al. 2010).
2. The cohesive riverbank soils are resistant to fluvial erosion and significant erosion is not expected for flows below $565 \text{ m}^3/\text{s}$ (20,000 cfs).
3. Soil permeability values measured in situ and in the laboratory differed by several orders of magnitude. The results from the in situ tests best matched the observations from the groundwater table monitoring.
4. The riverbanks at the study sites are stable in their present condition with regards to large scale failures. This result does not preclude the occurrence of occasional failure events over the lengthy river reach.
5. Small scale failures produce lower factors of safety especially in the presence of tension cracks.
6. The step-down scenario described in the lower Roanoke River Betterment Plan does not have an adverse effect on riverbank stability.
7. A flow rate of $990 \text{ m}^3/\text{s}$ (35,000 cfs) will result in overbank flow throughout much of the lower Roanoke River. This flow condition will not result in an increase in instability of the riverbanks compared to steady flow bankfull conditions. The present simplified numerical approach is not able to determine the effects of the designated overbank flow on fluvial erosion. This is a very challenging problem requiring more advanced and elaborate numerical simulations of fluid flow along with more detailed information about floodplain topography and roughness.

1. Introduction

This study investigates the effects of reservoir releases on riverbank erosion and stability on the downstream channel. The objective is to assess the impact of different discharge scenarios on fluvial erosion and stability of the riverbank. Using the field conditions and flow releases on the lower Roanoke River in eastern North Carolina (Fig. 1.1), numerical models of hydraulic and geotechnical processes related to the riverbanks were developed. Extensive field and laboratory tests provided the necessary inputs to build the models. The field work focused on five study sites on a reach of the lower Roanoke River below the Roanoke Rapids Dam. As shown in Figure 1.1, three of these sites correspond to location where erosion pins were installed (see Hupp et al. 2009). The sites were selected to represent a variety of different geotechnical and hydraulic characteristics found on the lower Roanoke River. Further information on the study sites and field work can be found in Petrie et al. (2009).

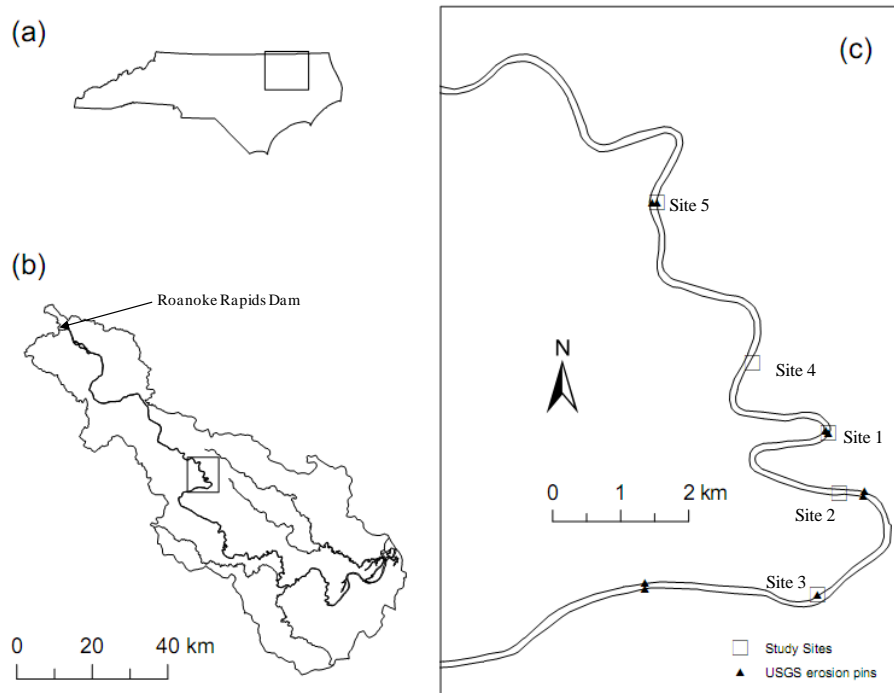


Figure 1.1. (a) North Carolina with a box showing the location of the Roanoke River watershed that falls within North Carolina. (b) The Roanoke River watershed below the Roanoke Rapids Dam with a box showing the location of the study reach. (c) The study reach on the lower Roanoke River.

Details of the work for this study completed through December 2009 is provided in Petrie et al. (2009). The major conclusions from this report are summarized as follows.

1. Steady flows of $310 \text{ m}^3/\text{s}$ (11,000 cfs) and below do not result in significant fluvial erosion.
2. Steady flows of $565 \text{ m}^3/\text{s}$ (20,000 cfs) were found to generate some fluvial erosion.
3. Mass failure was not predicted under a steady flow of $565 \text{ m}^3/\text{s}$ (20,000 cfs) for durations up to eight weeks. However due to cumulative erosion for several flow events, the stability of the bank will continue to decrease which may eventually result in failure.
4. Rapid drawdown conditions after sustained high flows could generate mass failure in low permeability soils.
5. Short-term peaking does not increase riverbank instability when compared with the steady flow cases.
6. The most critical flow scenarios in terms of bank erosion and stability result from flood control operations.

Based on limitations of the field data and numerical modeling results, it was determined that additional work was necessary to verify and extend these results. The main components of this additional work are further tests for soil permeability and erodibility and improvements to the numerical models. A site visit was conducted in May 2010 to obtain additional jet tests for soil erodibility and field tests for soil permeability. Approximately one month was spent carrying out additional laboratory tests for permeability in the spring of 2010. The slope stability models were updated using the results of the permeability tests. Additional models were also created to include all five study sites. The computational fluid dynamics (CFD) models of the river flow were also modified. Among the changes were an improved representation of the natural channel geometry, particularly for the meander bend site, and a more efficient numerical mesh. The geometry and numerical mesh were created using a newly-acquired software package ICEM-CFD (ANSYS, Inc., Canonsburg, PA). ICEM-CFD is a state-of-the-art CFD preprocessor that is particularly well suited to handle complex geometries, such as those encountered in natural rivers.

In addition to the work described above, two new issues were considered. The first of these issues was the step down flow regime following flood control releases. The objective is to determine an appropriate step down regime to minimize riverbank erosion and mass failure. Next, the effect of increasing the flood control discharge from $565 \text{ m}^3/\text{s}$ (20,000 cfs) to $990 \text{ m}^3/\text{s}$ (35,000 cfs) was also considered. The objective was to determine the effects of overbanks flow on riverbank stability in an approximate way. Given the additional complexity of overbank flows, more precise results will require considerably greater effort, including more information about the floodplain roughness and topography as well as a more advanced three-dimensional numerical model. Further details of the analyses can be found in the following chapters.

2. Fluvial Erosion of Cohesive Riverbanks

To calculate soil erosion, three basic components must be identified and quantified: (i) the eroding force applied to the soil by the flowing water, (ii) the resistance of the soil to the eroding force, and (iii) a threshold condition beyond which erosion commences (Annandale 2006). The resistance to erosion of cohesive soils, such as those found on the banks of the lower Roanoke River, is mainly due to electrochemical inter-particle forces. These complex forces are dependent on physical and chemical properties of the soil, eroding water, and pore water. Due to the difficulty in accounting for the large number of variables that contribute to cohesive soil erodibility, methods to determine erosion rates remain largely empirical. Among the most widely used mathematical models for cohesive soil erosion is the linear excess shear stress equation (Julian & Torres 2006):

$$\begin{aligned} \varepsilon &= 0 & \text{when } \tau_o < \tau_c \\ \varepsilon &= k_d(\tau_o - \tau_c) & \text{when } \tau_o > \tau_c \end{aligned} \quad (2.1)$$

where, ε = linear erosion rate (m/s)

k_d = erodibility coefficient ($\text{m}^3/\text{N}\cdot\text{s}$)

τ_o = shear stress applied by the flowing water (Pa)

τ_c = critical shear stress of soil (Pa)

The critical shear stress, τ_c , represents the threshold condition. Any applied shear stress below τ_c causes no erosion, while erosion commences once the applied shear stress exceeds τ_c . The erodibility coefficient, k_d , determines the rate of erosion once the critical shear stress is exceeded. This coefficient accounts for the effects of the inter-particle cohesive forces on erosion.

A number of approaches have been introduced to measure the erodibility of cohesive riverbank soils in laboratories and field sites, including the use of laboratory flumes (e.g. Arulanandan et al. 1980, Akahori et al. 2008) and specialized devices (e.g. Briaud et al. 2001, Hanson & Cook 2004). For the lower Roanoke River, an in situ technique is preferred due to the difficulty of removing and transporting the large number of soil samples required for laboratory testing. Of the few available techniques for in situ determination of soil erosion, the jet erosion test

developed by the U. S. Department of Agriculture – Agricultural Research Service was selected. The jet erosion test, often referred to simply as the jet test, applies a submerged jet of water to erode the surface soil and uses the evolution of the scour hole over time to determine the erodibility parameters of the excess shear stress equation (k_d and τ_c). The jet test has been applied to a number of studies in both the laboratory (e.g. Hanson & Cook 2004, Charonko 2010) and the field (e.g. Hanson & Simon 2001, Wynn 2004).

2.1 Overview of the Jet Test

The jet test procedure involves shooting a submerged jet of water perpendicular to the surface of the soil. When the jet hits the soil, it disperses radially, applying a shear stress to the soil surface. This shear stress causes the soil to erode and, thus, a scour hole is created. A detailed diagram of the impinging jet is provided in Figure 2.1. The increase in depth of the scour over time is measured. Analytical methods are then used to determine the erodibility parameters τ_c and k_d from the raw data. The method used in this report follows guidelines described by Hanson & Cook (2004).

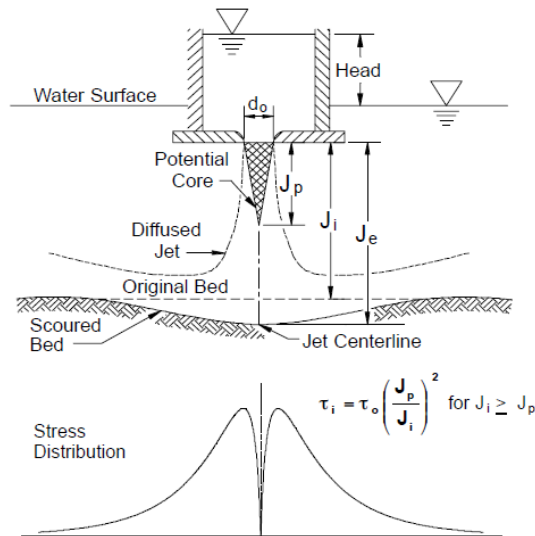


Figure 2.1. Diagram of jet, scour, and relative shear stress distribution (Hanson & Cook 2004).

The jet test apparatus used in the field is shown in Figure 2.2. It is comprised of an adjustable head tank, submergence tank, jet tube and nozzle, and a point gage for measuring scour depth.

Water is pumped to the adjustable head tank, which is elevated above the rest of the apparatus, and the tank provides a constant elevation head for flow to the jet tube. Water flows down from the head tank into the jet tube, and the difference in elevation creates a pressure jet. The jet flows from the jet tube through a nozzle and into the submergence tank, where it impinges on the soil. The jet tube is secured to the submergence tank, a circular ring that is hammered into the ground flush with the soil surface. A point gage is located in the center of the jet tube and is used to measure maximum scour depth at any given time.



Figure 2.2. Jet test apparatus installed at Site 1 during testing in May, 2010.

Prior to testing, a smooth soil surface was prepared by clearing away any mounds or clumps of soil as well as any vegetation. Once the soil was cleared, the submergence tank was secured to the ground via its base ring and use of a hammer. All other components were attached as described above, and a gas-powered pump was used to transfer water from the river to the head tank. The submergence tank was filled with water carefully by using cups or a bucket to minimize disturbance to the soil. Before starting the jet, a measurement of the initial soil surface depth was made with the point gage. The jet was turned on for 9 intervals of 5 minutes, a total of 45 minutes for each test. After every 5 minutes, a measurement was taken of the soil surface depth. Pressure readings were also taken to determine the velocity of the jet.

The amount of total scour after each 5 minute interval was measured using the point gage readings. Theoretically, scour will reach a maximum depth only if the test is allowed to run for an infinite amount of time. This is because as the soil surface erodes, the distance from the jet origin increases, therefore decreasing the impact of the jet. Eventually, erosion stops because the shear stress applied by the jet is no longer sufficient to remove soil. The theoretical scour depth at which this happens is referred to as the equilibrium scour depth, J_e , and is determined using a mathematical process described by Blaisdell et al. (1981). The shear stress generated by the jet at this depth is equal to the critical shear stress, τ_c , and is the threshold condition for erosion. The shear stress applied by the jet can be estimated as a function of scour depth (Beltaos & Rajaratnam 1974), so that the critical shear stress, τ_c , can be calculated after determining the equilibrium scour depth, J_e .

The excess shear equation (equation 2.1) provides a procedure to solve for the erodibility constant, k_d . A regression method is used as described in Hanson & Cook (1997). A spreadsheet developed by Hanson & Cook (2004) combines methods for determining J_e , τ_c , and k_d from the raw field data. This spreadsheet was used to calculate the soil parameters: J_e and, subsequently, τ_c and k_d .

2.2 Discussion of Results

A total of 31 in situ jet test experiments were performed from August 2007 through May 2010 at several locations on the lower Roanoke River. About half the total tests (14) were performed in May 2010. After removing incomplete tests and tests on non-representative soil types, 26 tests were deemed representative of the study sites. These 26 experiments are analyzed in further detail below. Tests were performed at all five study sites along the LRR, and the results are categorized by both site and soil type in Table 2.1. Using the Unified Soil Classification System (USCS), the soil types include low plasticity clay (CL), low plasticity silt (ML), and high plasticity silt (MH). While no consistent relationship has been observed between τ_c and k_d , the results are often presented in a log-log graph as seen in Figure 2.3. From the table and figure, it can be seen that the jet test results show a wide range of values for the critical shear stress, τ_c ,

and erodibility coefficient, k_d . Additionally, no clear trend is observed for either study sites or soil types.

The variability of both the critical shear stress and erodibility coefficient determined with the jet test is well documented in the literature (Wynn et al. 2008, Clark & Wynn 2007, Thoman & Niezgoda 2008, Hanson & Cook 1997). Variability in the predicted erodibility parameters can be due to a number of site-related or equipment factors. However, the recent work of Charonko (2010) suggests that the jet test results are repeatable, indicating that differences in results can be attributed to variations in site conditions. Natural riverbank soils can vary widely (Nam et al. 2010), thus a single jet test cannot be considered entirely representative of a site.

Table 2.1. Descriptive Statistics for k_d and τ_c

	$k_d \times 10^{-7} (\text{m}^3 \text{N}^{-1} \text{s}^{-1})$				τ_c (Pa)			
	mean	median	range	std dev	mean	median	range	std dev
Soil								
CL	15.69	5.96	57.35	20.93	5.53	4.83	13.82	4.69
MH	6.19	3.98	22.33	6.52	10.21	11.49	20.97	7.34
ML	9.16	7.36	20.16	7.00	6.15	8.51	10.50	4.84
Site								
1	3.90	4.00	5.58	1.60	9.55	6.90	20.37	7.15
2	25.04	9.96	57.35	31.51	6.59	3.82	13.82	7.32
3	13.51	12.69	18.26	6.65	4.79	1.63	10.48	5.43
4	11.52	11.52	17.60	12.45	7.98	7.98	3.94	2.79
5	10.58	7.36	20.16	10.46	6.85	8.51	9.67	5.04
Total	9.55	4.73	59.56	12.31	7.86	6.50	21.14	6.29

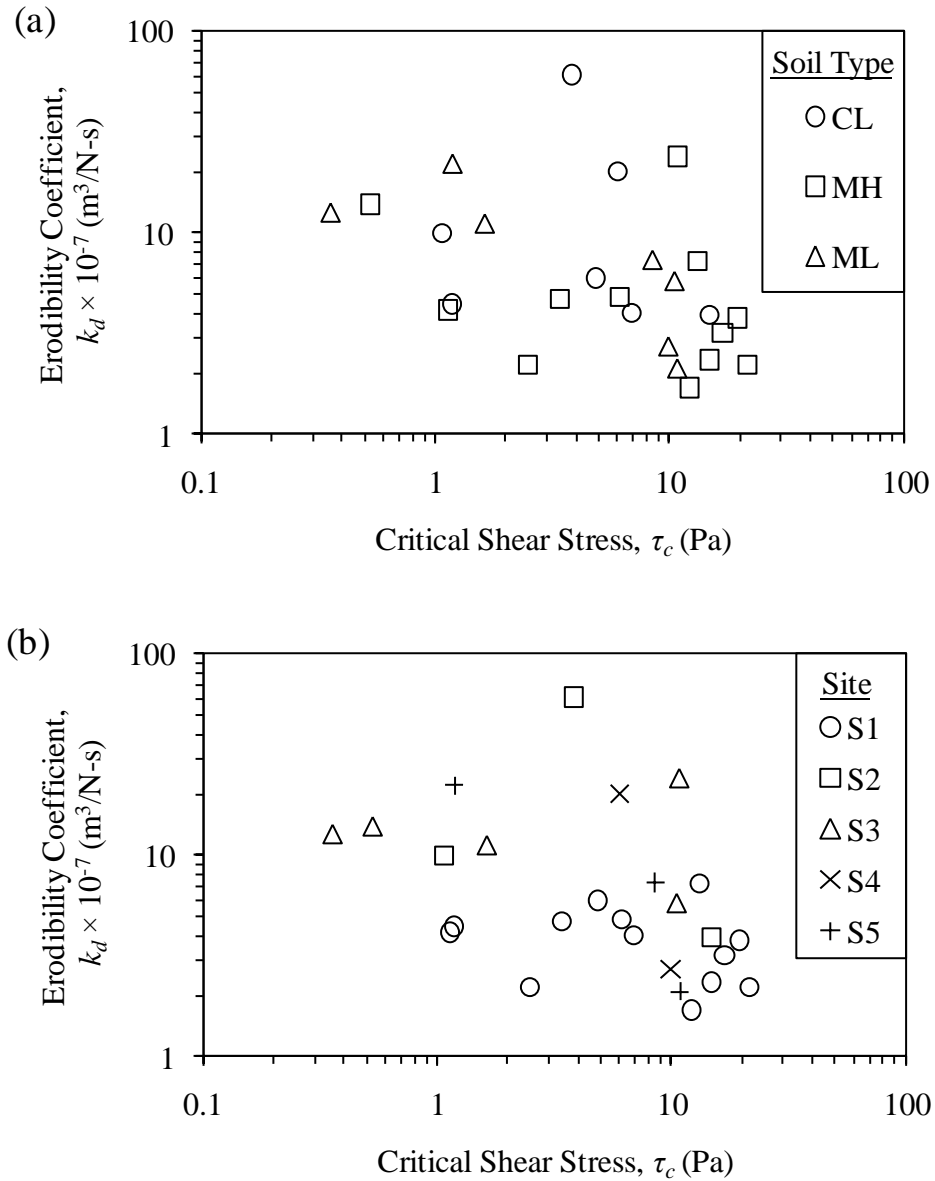


Figure 2.3. Critical shear stress, τ_c , and erodibility coefficient, k_d organized by (a) soil type and (b) study site.

While no guidelines exist for the appropriate number of jet tests to adequately describe a site, Hanson & Cook (2004) state that as the sample size increases, the average values of the erodibility parameters become more representative of the site. The number of tests performed at each site varied depending on the soil types present at each location as well as accessibility to the banks. A summary of sample size by location and soil type is shown in Table 2.2. The total

of 26 samples compares favorably with the sample sizes reported in many studies (e.g. Darby et al. 2007, Hanson & Cook 2004).

Table 2.2. Sample size by site and soil type

Site	No. of Tests	Soil Type	No. of Tests
1	13	CL	7
2	3	ML	7
3	5	MH	12
4	2	Total	26
5	3		
Total	26		

Due to the wide range of values seen in the test results, an appropriate analysis technique must be selected. The median values are less likely to be influenced by outliers and extreme events and, thus, are more appropriate than the mean for representing the erodibility parameters (Marques de Sá 2003). However, even the median value for the critical shear is higher than the shear stress applied to the banks as predicted by the CFD simulations at 565 m³/s (20,000 cfs). This result indicates that large amounts of erosion should not be expected for flow rates of 565 m³/s (20,000 cfs) or less. However, as indicated by the erosion data of Hupp et al. (2009) as well as field observations, some erosion does occur. To account for this erosion, the minimum critical shear stress from tests in each soil layer is used to provide a conservative estimate. The estimated rate of erosion would not occur over the entire bank, but rather would be limited to locations where the soil more susceptible to erosion is present. The use of this value provides a “worst-case scenario” estimate for fluvial erosion.

3. Soil Permeability

Petrie et al. (2009) found that the variability of permeability was very wide and that the permeability measured in the laboratory was much lower than what was estimated from in situ groundwater table observations. Both the seepage and riverbank stability modeling were analyzed for different permeability ranges and the riverbank stability also considered both high and low values of permeability. Permeability is a crucial input parameter that affects the seepage and stability analysis, especially under time dependent cases such as rapid drawdown. Thus, further investigation of the permeability of riverbank soils was performed. Three different methods were considered in addition to the traditional laboratory constant head permeability tests.

(1) Oedometer test

The oedometer test simulates one dimensional consolidation using either incremental loading or controlled-strain loading method. The incremental loading method is a standard method defined in ASTM D 2435 (2004). The incremental loading method applies a constant load for a time period (typically 24 hours), and vertical deformation is measured and plotted in a semi-logarithmic graph. After determining 90% or 50% consolidation points under a certain load in the graph, the 100% consolidation point, where the primary consolidation is completed, can be determined. After performing the same procedures for different loads, void ratio vs. consolidation pressure curve (e-log P curve) can be obtained by plotting void ratio at the end of consolidation and load, and preconsolidation stress can be determined. During the process, permeability at each loading stage can be determined by the equations shown below.

$$\begin{aligned} k &= c_v m_v \gamma_w \\ &= c_v \frac{a_v}{1+e} \gamma_w \\ &= \frac{T_v \gamma_w}{t \Delta \sigma} \frac{\Delta e}{1+e} H^2 \end{aligned} \tag{3.1}$$

Where, c_v = coefficient of consolidation $c_v = \frac{T_v H^2}{t}$, m_v = coefficient of volume compressibility

$m_v = \frac{a_v}{1+e}$, and a_v = coefficient of consolidation $a_v = -\frac{de}{dp}$, H = drainage length.

(2) Auger hole method

The auger hole method is a quick and simple but reliable test that can be easily performed in the field. It was originally proposed by Diserens in 1932 and later improved by many researchers (van Beers 1983). The auger hole method requires a monitoring well to be drilled below the ground water table. Once the observation well is created and the water table inside the well reaches equilibrium, the test starts by removing all the water in the hole. The water in the hole then rises until it returns to the initial stage, and the time required to reach the equilibrium again is measured. As stated previously, the auger hole method is very simple and efficient technique to estimate saturated hydraulic conductivity in the field without sophisticated equipment. As shown in Figure 3.1, the only parameters required for an auger hole test are hole dimensions (diameter, depth), the location of water table in the hole, and the location of the impermeable layer below the hole. Some additional benefits of the test are that several tests can be done easily at the same time, disturbed and undisturbed soil samples can be obtained, and the soil profile can be identified during the test.

The results of the auger hole test can be easily interpreted using plots proposed by Boumans (1953) or using an equation proposed by Ernst (1950). The graphical method is known to be more accurate, but the equation approach is preferable when the figures are not available on hand or for specific field conditions (van Beers 1983).

The following equation is for homogeneous soil with an impermeable layer existing $0.5 \times (\text{distance from the water table to the bottom of the auger hole})$ or more below the bottom of the auger hole (Ernst, 1950).

$$k = \frac{4000}{\left(\frac{H}{r} + 20\right) \left(2 - \frac{y}{H}\right)} \frac{r \Delta y}{y \Delta t} \quad (3.2)$$

Where, k = hydraulic conductivity and the other variables are as described in Figure 3.1.

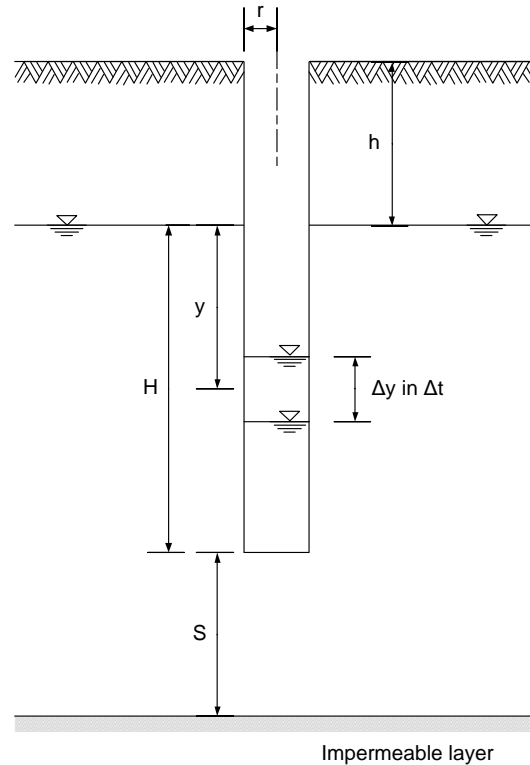


Figure 3.1. Schematic diagram of the auger hole method.

(3) Guelph permeameter

The Guelph permeameter method is an in situ test to measure saturated hydraulic conductivity of unsaturated soils using a Mariotte siphon reservoir, and is a type of field technique variously known as a constant head well permeameter, borehole permeameter, well permeameter, inverse auger hole, shallow well pump-in, or dry auger hole methods (Bagarello et al. 1999).

Calculation of soil permeability using the data from the Guelph permeameter was made by using a two-head analysis. A few cases presented a negative value of permeability. This could be caused by heterogeneous soils in the field, and a one-head analysis can be used instead (Soilmoisture Equipment Corp. 2006).



Figure 3.2. Guelph permeameter testing device installed on the lower Roanoke River.

(4) Ground water table observation

Additional laboratory and in situ tests were performed to determine the hydraulic conductivity required for seepage analysis. It was found that there are differences of several orders of magnitude between the laboratory and in situ test results. To confirm the validity of the test results, the locations of the ground water table with different values of hydraulic conductivity were predicted by finite element modeling, and compared with the measured ground water table in the field. The models with in situ permeability coefficients provide better predictions of the ground water table locations for different flow scenarios, which suggests that the in situ hydraulic conductivity is more reasonable and appropriate for transient seepage modeling.

Table 3.1. Average values of permeability from different methods

Site No.	USCS Soil Type	Coefficient of Permeability (cm/sec)			
		Laboratory		In Situ	
		$K_{sat\ CH}$	$K_{sat\ CON}$	$K_{sat\ AH}$	$K_{sat\ GP}$
S1	CL	6.69×10^{-8}	7.32×10^{-8}		
S1	MH	2.30×10^{-7}	9.01×10^{-7}	1.35×10^{-3}	4.11×10^{-6}
S1	CL	1.03×10^{-7}	1.26×10^{-7}	5.70×10^{-4}	1.45×10^{-6}
S3	ML		7.94×10^{-6}	9.71×10^{-6}	1.45×10^{-5}
S4	ML		1.72×10^{-6}		
S4*	ML		2.73×10^{-5}		
S5	ML	5.90×10^{-7}	3.57×10^{-6}	4.89×10^{-4}	2.71×10^{-5}
S5	CL	7.68×10^{-7}	8.11×10^{-6}		

* horizontal permeability

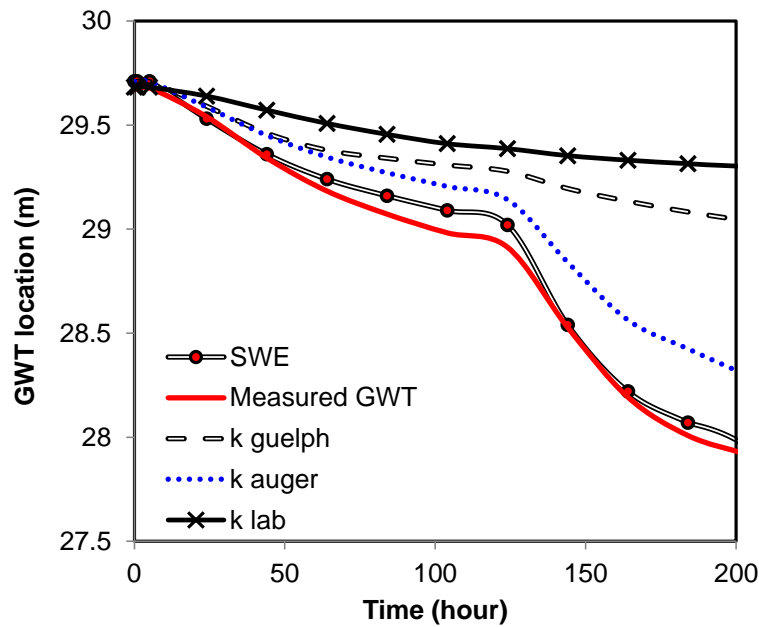


Figure 3.3. GWT modeling with different permeability values and field measured results at Site 1 (June 20 – 29, 2009).

Table 3.1 shows that the permeability values from different methods show a wide range of variation, and, in some cases, the in situ values were much larger than the lab values. The differences among the different laboratory tests were about 1 to 10 times in a same type of soil, whereas those in the in situ tests were between 1 to 400 times. The differences of the permeability between the laboratory tests and field tests were even larger than these, varying up to 10^4 times in one case. However, the difference between the average laboratory permeability and the average in situ permeability, except the largest in situ permeability, was in between 1 to 500 times. The larger differences resulted from higher permeability values obtained by auger hole tests. However, the saturated permeability coefficients determined by the auger hole method provided the closest values to the field observations with the GWT sensors. Although there are several parameters and boundary conditions affecting the modeling results, the permeability is the most critical parameter in this case. Thus, the seepage conditions in the riverbanks of the lower Roanoke River seem to be dominated by soils with high permeability, probably due to preferential flow. Similar observations at a natural levee in the Atchafalaya River Basin, LA, were reported by Newman (2010), and the importance of preferential flows in wetlands has been studied recently by Harvey & Nuttle (1995) and Fitzgerald et al. (2003). The clay was very hard when it was dry, and surface cracks and pores were observed as shown in Figure 3.4. The clay soil also seems to have structures as a thin layer of soil often became dislodged when the jet test ring was removed.



(a) Surface condition of CL soil

(b) clean cut of soil along jet test ring

Figure 3.4. Cracks, pores and proof of structured soils after jet test.

(5) GWT location

The initial location of the groundwater table (GWT) is an important input parameter in transient seepage analysis and, ultimately, affects the results of slope stability modeling. Petrie et al. (2009) simply assumed 5 different initial locations for different flow conditions, and the modeling results showed that bank stability increases as GWT location decreases. These results are expected as the shear strength of soil is expected to increase as the degree of saturation decreases in unsaturated soils. However, the initial boundary condition for the GWT directly affects the location of the phreatic surface in transient seepage analysis, and thus, needs to be defined as realistically as possible. In other words, if the initial boundary condition does not represent the actual site conditions, the modeling results cannot be compared to the GWT observed in the GWT monitoring holes.

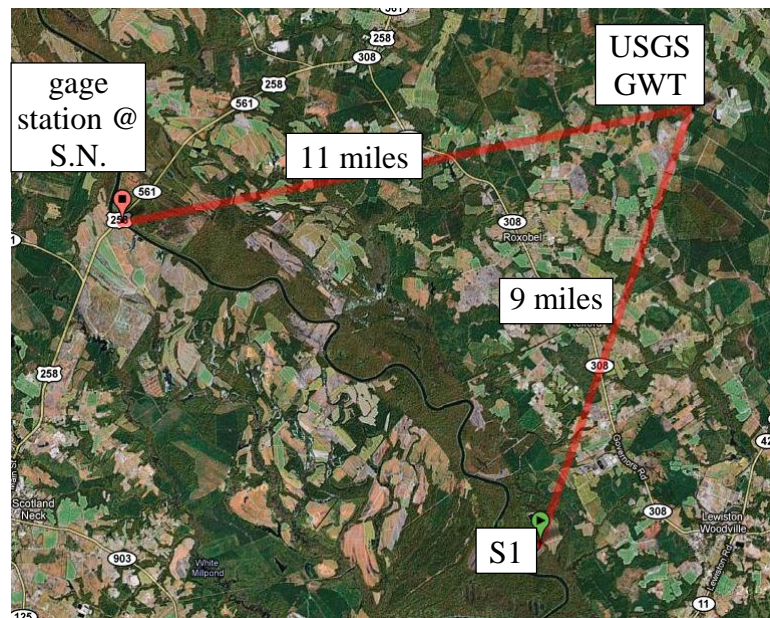


Figure 3.5. Location of USGS GWT measurement data.

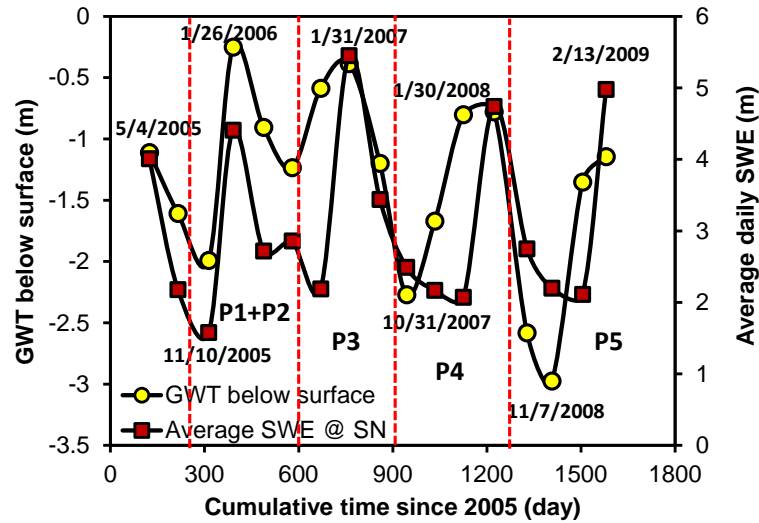


Figure 3.6. Variation of ground water table and water surface elevation between 2005 and 2009 monitored by USGS GWT station at Roxobel, NC.

The locations of GWT and WSE measurements operated by the USGS are shown in Figure 3.5 and the measured GWT data are compared to the WSE in Figure 3.6. The GWT information was measured during site visits, whereas the stream flow data is the average WSE on the same day that GWT was measured. The changes of GWT in Figure 3.6 are not expected to be the results of instantaneous responses to changes in dam discharge or WSE changes. They are more likely seasonal elevations which are influenced by the long term WSE rather than fluctuating or peaking discharge. Thus, the comparison between the GWT and average WSE seems to be reasonable, and the results seen in Figure 3.6 can be used to determine the initial location of GWT for steady state seepage modeling. Due to the fact that the WSE is affected by the preceding discharge rate, a WSE does not always correspond to a GWT. As demonstrated in Figure 3.6, the corresponding GWT would be different depending on the field conditions at the time of measurement.

In conclusion, one initial GWT location (left boundary condition) corresponding to one flow rate is determined as presented in Table 3.2. However, it is assumed that the flow condition has lasted long enough to create steady state flow condition.

Table 3.2. Locations of far left boundary condition and WSE for different steady state flow rates.

	Steady state flow rate (cfs)						
	2,000	5,000	8,000	11,000	15,000	20,000	35,000
WSE location (m)	24.2	25.7	26.8	27.7	28.6	29.7	31
Left boundary condition (m)	27.5	28	28.5	29	29.4	29.7	30

Bank top elevation = 30m

4. Computational Fluid Dynamics

Fluid flows are governed by a set of nonlinear partial differential equations known as the Navier-Stokes equations. While solutions can be found for some simple cases, no closed-form solution for the Navier-Stokes equations exists for most practical engineering flows. Computational fluid dynamics (CFD) employs numerical methods to solve the Navier-Stokes equations (Ferziger & Perić 2002). In general, the flow domain is divided into many small elements and the non-linear partial differential equations that govern fluid motion are approximated with a system of algebraic equations. Due to advancements in computational resources, CFD has grown rapidly over the last twenty years and has found a wide range of applications. Rivers and other environmental flows are a relatively new application for CFD that is currently receiving much research interest (e.g. Bates et al. 2005, Shen & Diplas 2008 & 2010).

The three dimensional computations for this study were carried out with FLUENT (ANSYS, Inc., Canonsburg, PA), a commercially available CFD code. FLUENT was selected because it provides a number of options for numerical methods and accepts most common varieties of meshes. The solutions are second-order accurate and the SIMPLE method was used for pressure-velocity coupling (Patankar 1980). The pre-processing of the geometry, including mesh generation, was performed with ICEM-CFD (ANSYS, Inc.). The ANSYS, Inc. CFD package represents the latest and most sophisticated technology on 3D numerical flow simulation currently available in the industry. Additionally, FLUENT has been applied to a number of studies on open channel flows (e.g. Hodkinson 1996, Strom et al. 2007).

4.1 Straight Reach

Site 5 (Fig. 1.1) was used as the representative straight reach site for CFD modeling. The cross-section geometry was generated by merging ADCP field measurements of bathymetry and aerial LiDAR images of the floodplains. The domain for the numerical simulations is provided in Figure 4.1. The cross-section seen in the figure represents an improvement over the previous Site 5 CFD model (Petrie et al. 2009), where the cross-section was approximated as a trapezoid. The new geometry should provide improved predictions of flow quantities such as the distributions of velocity and boundary shear stress. The channel width at the water surface is about 110 m (360 ft) when the discharge is $565 \text{ m}^3/\text{s}$ (20,000 cfs).

The flow boundaries also shown in Figure 4.1 are: (i) the flow inlet, (ii) the flow outlet, (iii) the water surface, and (iv) channel boundary. The flow inlet and outlet are coupled using a periodic boundary condition with a specified mass flow rate. A periodic condition assumes that the flow entering and exiting the computational domain is the same (Tu et al. 2008). For straight prismatic reaches, the flow is typically assumed to be fully-developed and, therefore, periodic boundary conditions apply. The water surface is treated with a symmetry boundary condition, which assumes that no fluid is transported across the boundary. If the water surface is known, a symmetry boundary condition reduces the computational effort (Lane et al. 1999). The water surface location was determined a priori using steady state HEC-RAS simulations similar to the approach employed by Rüther et al. (2010). The channel boundary is treated as a no-slip wall boundary with uniform roughness of $k_s = 0.01$ m (0.33 ft) specified across the channel.

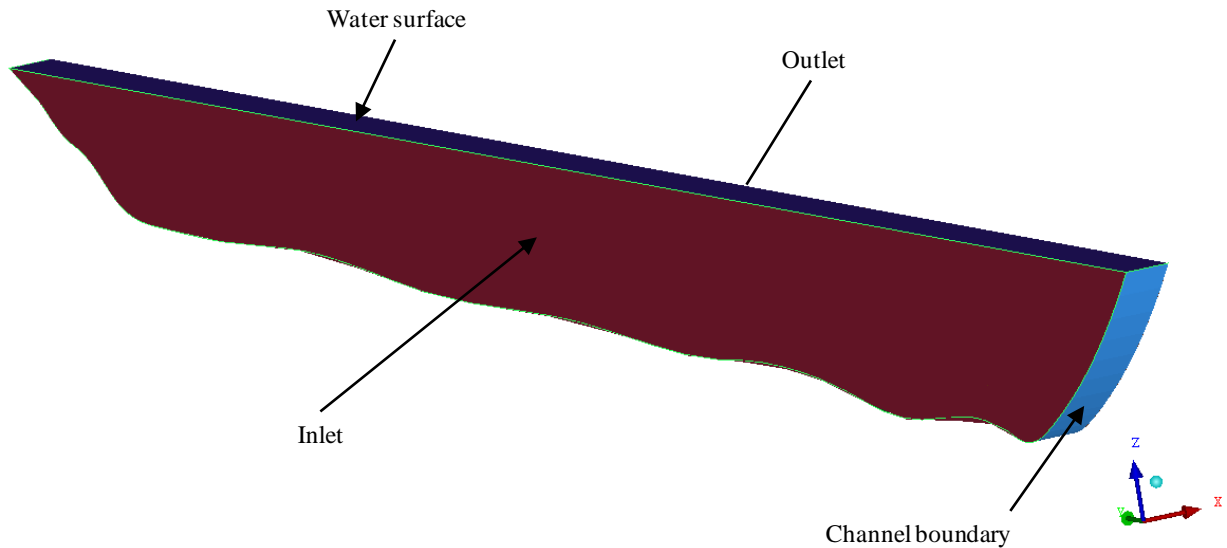


Figure 4.1. Domain and boundaries for Site 5 CFD simulations. Flow is in the positive x -direction.

The computational domain was discretized into hexahedral elements. The size of the elements ranged from about 0.0001 m (0.0003 ft) to 0.85 m (2.80 ft) depending on the proximity to the channel boundary. To accurately capture the large near-wall gradients, smaller elements are located adjacent to the wall boundary as shown in Figure 4.2. The maximum element widths are

located near the channel center. Due to the periodic boundary conditions, only a single element of arbitrary width is required in the direction of flow. The number of elements used is then dependent on the size of computational domain which, in turn, is determined by the flow rate. The computational mesh for a flow rate of $565 \text{ m}^3/\text{s}$ (20,000 cfs) contains 53,394 elements.

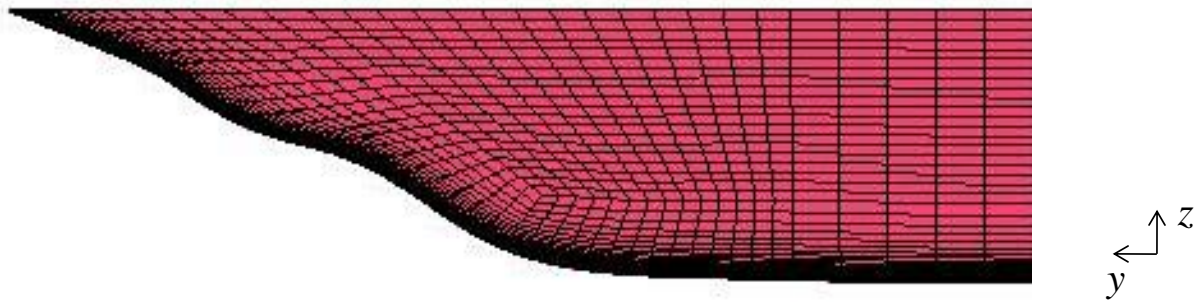


Figure 4.2. Numerical mesh at the left bank of Site 5 CFD simulations. The direction of flow is into the page.

To represent the effects of turbulence, the $k-\omega$ SST model was employed (Wilcox 2006). This model was selected for two primary reasons: (i) it is applicable to the entire flow domain, including the near-wall region, and (ii) has been shown to produce results in good agreement with experiments for open channel flows (Strom et al. 2007). The use of the $k-\omega$ SST model requires a very fine mesh in the near-wall region (see Fig. 4.2).

Figures 4.3 and 4.4 provide the distribution of boundary shear stress across the channel and contours of velocity magnitude, respectively. The boundary shear stress follows the expected pattern of low shear stresses applied to the banks which increase with flow depth towards the middle of the channel. The peak shear stress roughly corresponds to the largest flow depth in the channel. The highest velocities also occur in the vicinity of the deepest flows. The velocity distribution can be seen to follow a regular pattern with increasing velocity from the banks and channel bed towards the center of the channel (Chaudhry 2008).

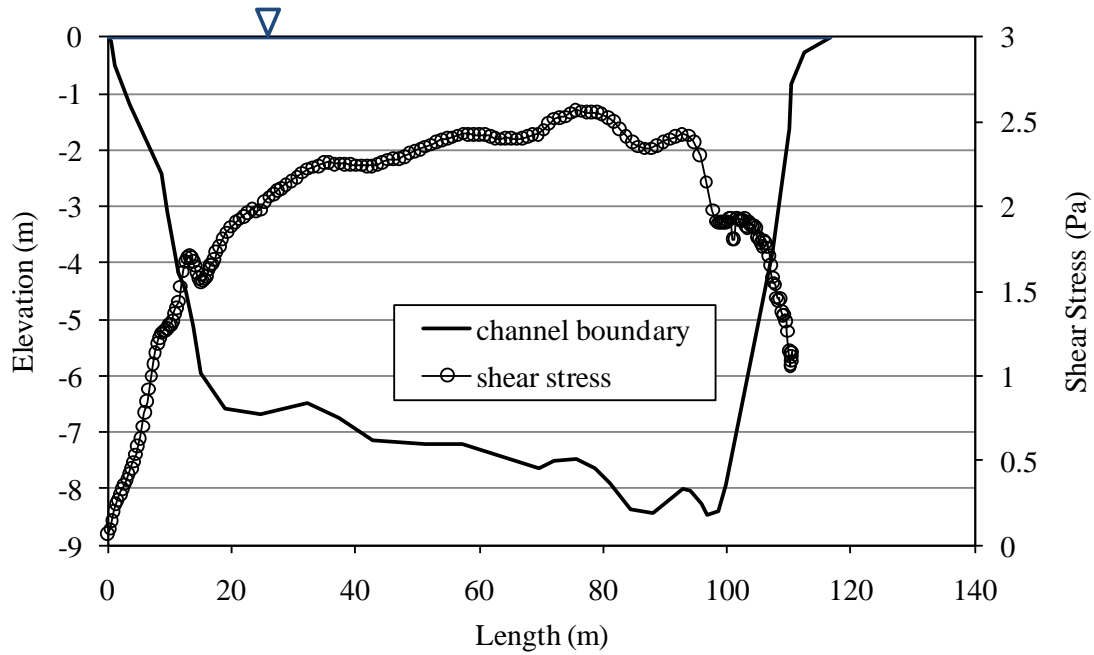
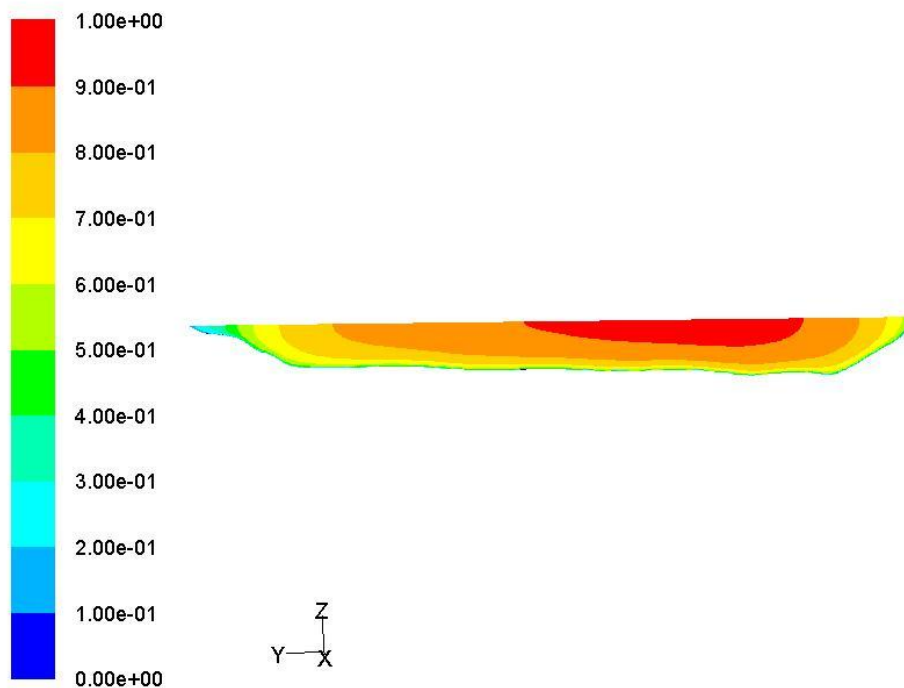


Figure 4.3. Boundary shear stress distribution at Site 5 for a flow rate of $565 \text{ m}^3/\text{s}$ (20,000 cfs).



Contours of Velocity Magnitude (m/s) Dec 17, 2010
ANSYS FLUENT 12.0 (3d, dp, pbns, sstk)

Figure 4.4. Contours of velocity magnitude at Site 5 for a flow rate of $565 \text{ m}^3/\text{s}$ (20,000 cfs). The direction of flow is into the page.

4.2 Meander Bend

Site 1 (Fig. 1.1) was used as the representative meander bend site for CFD modeling. The flow geometry was generated by merging ADCP field measurements of bathymetry and aerial LiDAR images of the floodplains. A view of the water surface for the numerical simulations is provided in Figure 4.5 along with an aerial photograph of Site 1. Figure 4.6 shows the channel banks and bed for the numerical flow domain.

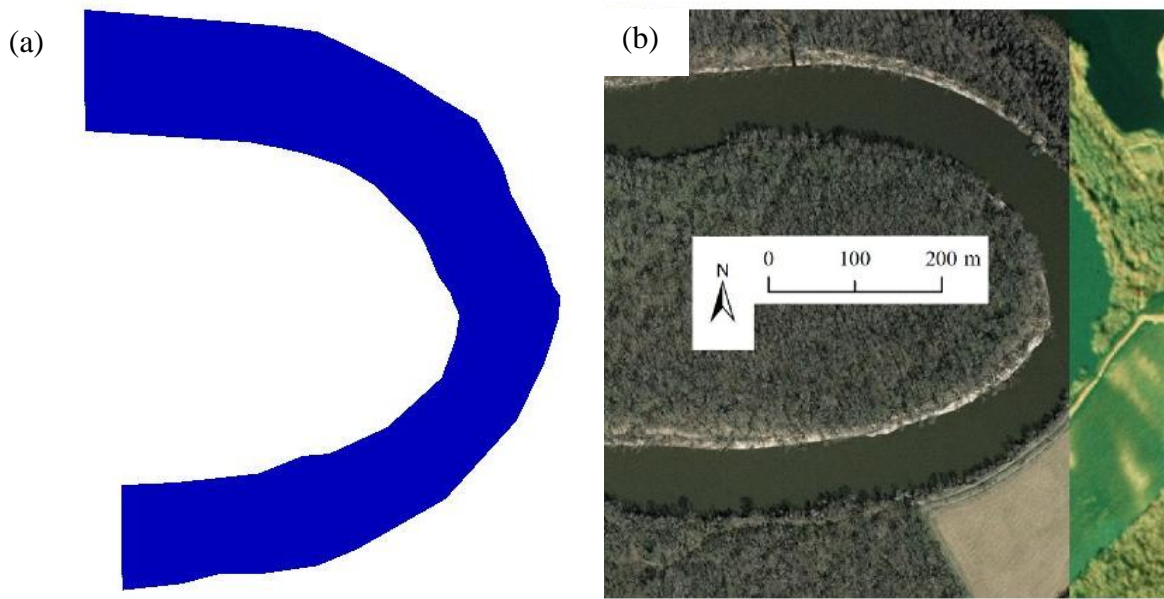


Figure 4.5. (a) Water surface geometry for CFD model of Site 1 and (b) aerial photograph of Site 1.

The flow boundaries are the same as for the straight reach, Site 5, and include (i) the flow inlet, (ii) the flow outlet, (iii) the water surface, and (iv) channel boundary. The boundary condition for the flow inlet is a velocity inlet, where the velocity at each location is specified. The inlet velocities were determined by treating the inlet cross-section as a straight reach and following the procedure presented in the previous section for Site 5. The outlet boundary condition is a pressure outlet, which requires the boundary to be placed far from areas where flow characteristics may change significantly. As with Site 5, the water surface is treated with a

symmetry boundary condition and the channel boundary is treated as a no-slip wall boundary with uniform roughness, $k_s = 0.01$ m (0.033 ft), specified for the channel bed and banks.

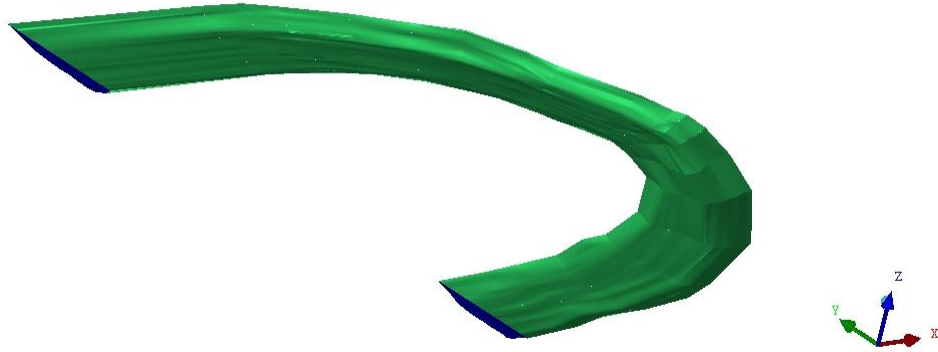


Figure 4.6. Channel geometry at Site 1.

The computational domain has a length of about 900 m and was discretized into hexahedral elements. The height of the elements is about 0.50 m (1.64 ft). The element size in the horizontal plane has a maximum size of about 2×2 m (6.56 \times 6.56 ft). To illustrate the numerical mesh, Figure 4.7 shows the mesh applied to the channel wall and two sample cross-sections. The region between the channel boundary and water surface is completely filled with hexahedral elements. The computational mesh for a flow rate of $565 \text{ m}^3/\text{s}$ (20,000 cfs) contains 917,232 elements.

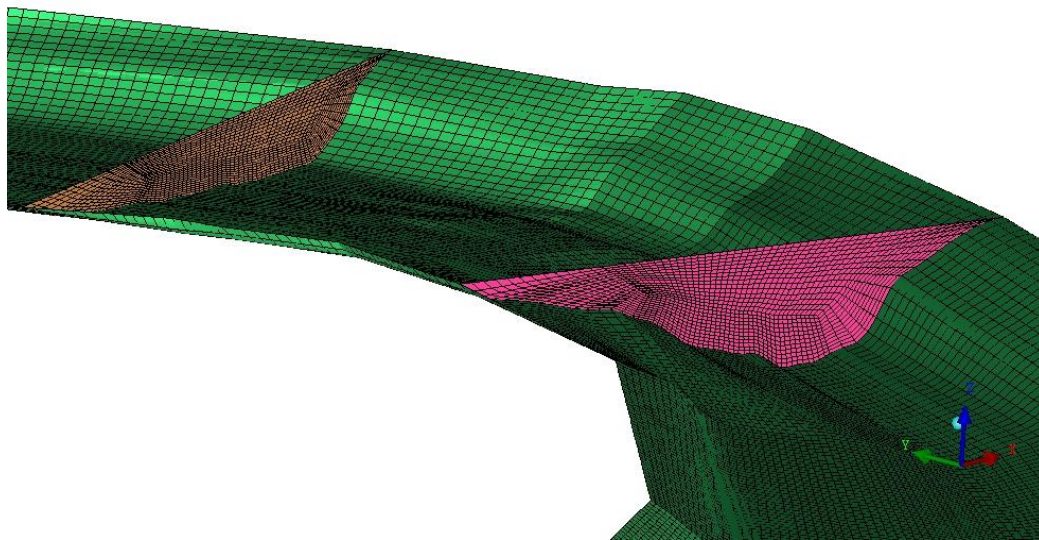


Figure 4.7. Example of the numerical mesh within the channel bend.

Due to the increased domain size, use the $k-\omega$ SST turbulence model would result in very large computational time. Instead the Renormalization group theory (RNG) $k-\varepsilon$ turbulence model with non-equilibrium wall functions was used to model the effects of turbulence on the mean flow. This approach has the ability to consider anisotropic turbulence that occurs in the near-wall region and in complex flow geometries, such as meander bends. A detail description of this modeling approach can be found in Yakhot & Orszag (1986) and Wilcox (2006).

The simulation was performed on a 2.0 GHz quad core workstation and required approximately 144 hours for convergence. Figure 4.8 shows contours of velocity magnitude at the water surface for a flow rate of $565 \text{ m}^3/\text{s}$ (20,000 cfs). It can be seen that a central core of high velocity moves from the inside bank towards the outer bank as the flow approaches the apex. Similar results have been seen in numerical simulations of laboratory flows (e.g. Stoesser et al. 2010b). This core of high velocity helps to apply a higher shear stress to the outer bank of the meander bend which can be seen in Figure 4.10 and 4.11. While the shear stress is generally higher on the outer bank, a core of high velocity near the bed generates the maximum shear stress. Due to the lower flow depths and velocity, the shear stress applied to the inner bank is less than that applied to the outer bank, as demonstrated in Figure 4.11. Secondary currents also play a role in increasing the shear stress applied to the outer bank. Evidence of secondary currents can be seen in Figure 4.12 in the form of the velocity dip (Chaudhry 2008). A comparison of Figures 4.4 and 4.12 illustrates the increased flow complexity found in meander bends.

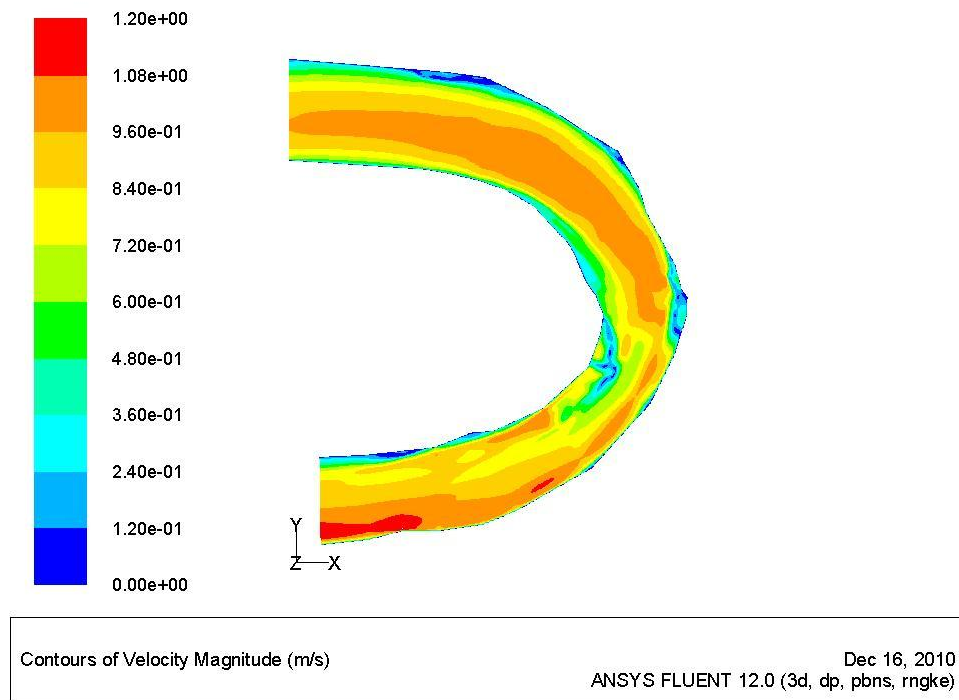


Figure 4.8. Contour plot of water surface velocity magnitude at Site 1 for a flow rate of $565 \text{ m}^3/\text{s}$ (20,000 cfs).

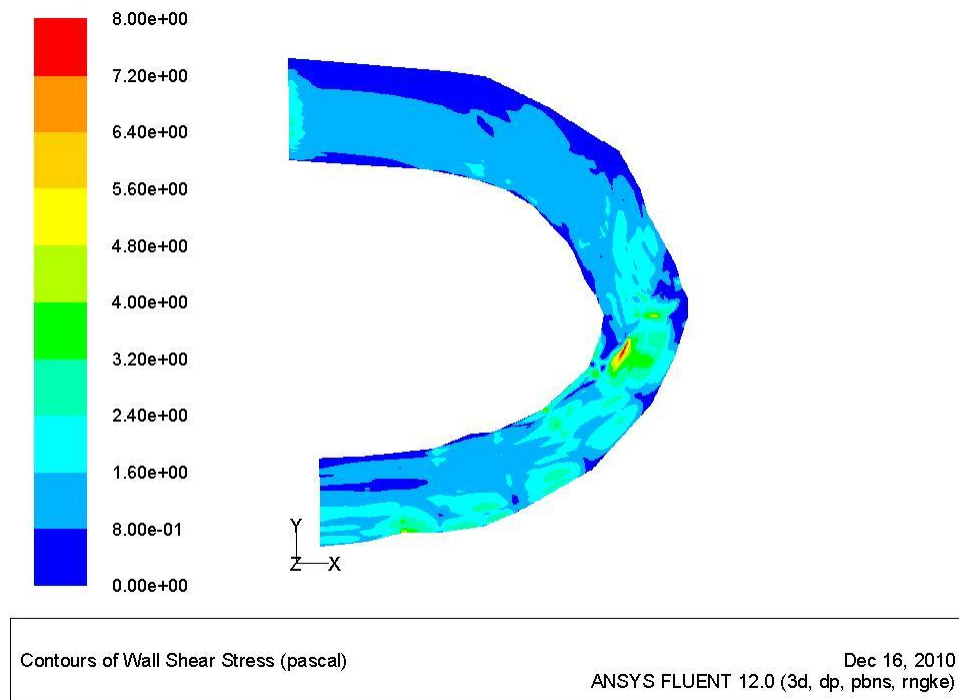


Figure 4.9. Contour plot of boundary shear stress at Site 1 for a flow rate of $565 \text{ m}^3/\text{s}$ (20,000 cfs).

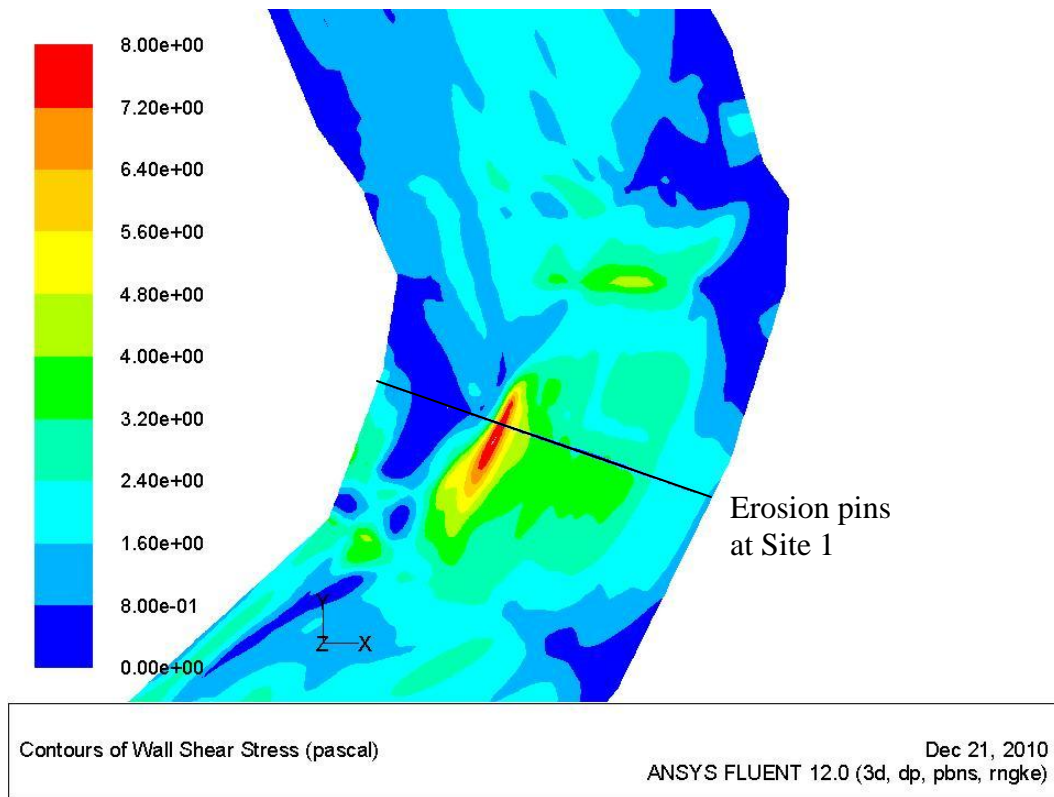


Figure 4.10. Boundary shear stress at the bend apex for a flow rate of $565 \text{ m}^3/\text{s}$ (20,000 cfs).

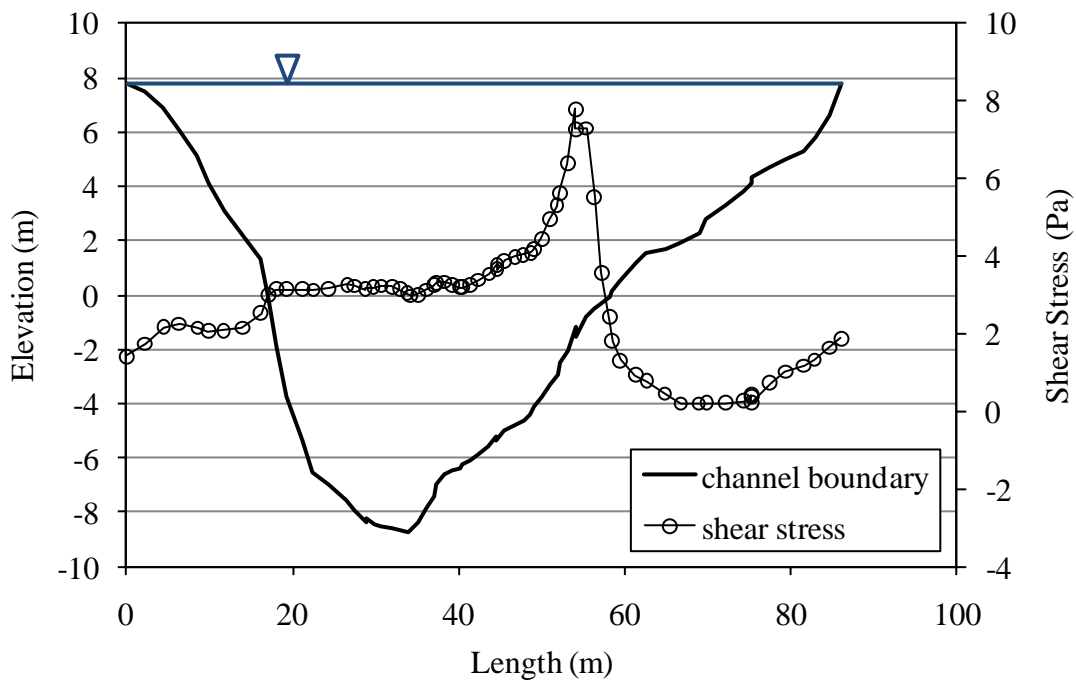
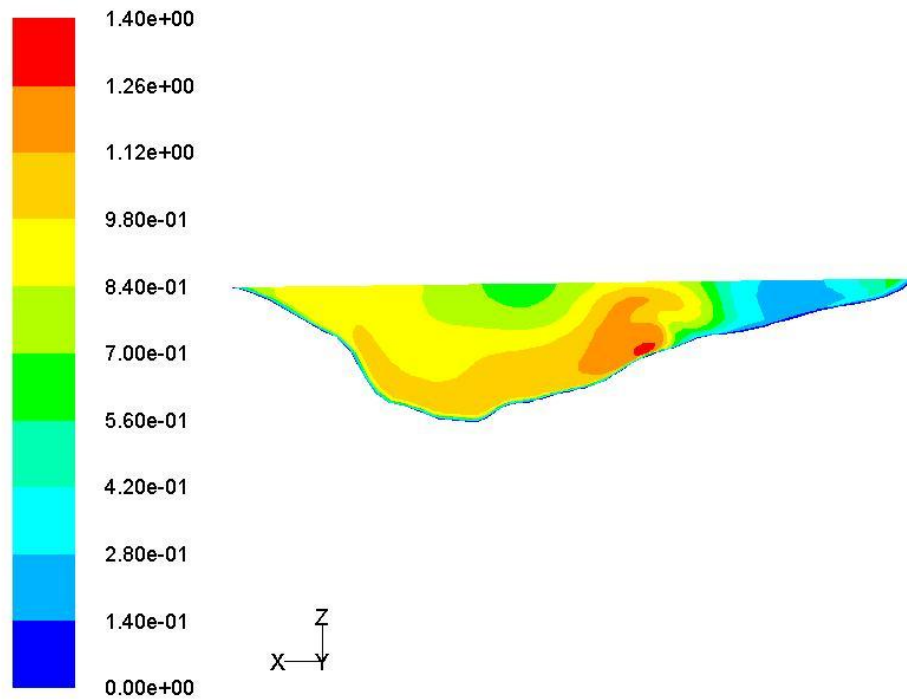


Figure 4.11. Distribution of boundary shear stress near the erosion pins at Site 1 for a flow rate of $565 \text{ m}^3/\text{s}$ (20,000 cfs). The direction of flow is into the page.



Contours of Velocity Magnitude (m/s)

Dec 16, 2010
ANSYS FLUENT 12.0 (3d, dp, pbns, rngke)

Figure 4.12. Contour plots of velocity magnitude near the erosion pins at Site 1 for a flow rate of $565 \text{ m}^3/\text{s}$ (20,000 cfs). The direction of flow is into the page.

5. Geotechnical Modeling

The geotechnical modeling of the lower Roanoke River consists of seepage analysis and slope stability analysis. The seepage analysis determines the pore pressure distribution in the riverbank, whereas the slope stability analysis determines the stability of the riverbank. Although each analysis is a separate process and has different critical factors, the results of the seepage analysis are required for slope stability analysis. Further background information on the seepage and slope stability analyses is available in Petrie et al. (2009).

(1) Seepage analysis

Seepage analysis is required to determine pore pressure condition in the riverbank, and can be used to determine the effective stress of the soil. Pore pressure changes with time are difficult to obtain analytically, but can be estimated with a finite element program. Input parameters for the finite element program were determined by laboratory and in situ tests, and the bank geometry was obtained from LiDAR and ADCP measurements. Steady state conditions are considered for seven flow rates: 56.6 m³/s (2,000 cfs), 140 m³/s (5,000 cfs), 225 m³/s (8,000 cfs), 310 m³/s (11,000 cfs), 425 m³/s (15,000 cfs), 565 m³/s (20,000 cfs), and 990 m³/s (35,000 cfs). Two major events, rapid drawdown and step-down scenario, were considered for transient analysis. Peaking releases from the reservoir are not considered because of the fact that the downstream WSE is insensitive to peaking (Petrie et al. 2009). Therefore, it can be regarded as a kind of drawdown case.

(2) Slope stability analysis

The stability of a slope is analyzed using the concept of a factor of safety (Duncan & Wright 2005).

$$\text{Factor of Safety} = \frac{\text{available shear strength}}{\text{equilibrium shear stress}} \quad (5.1)$$

The equilibrium shear stress represents the point beyond which any additional shear stress will result in failure. Slope stability is determined with the limit equilibrium method (LEM) considering unsaturated soil conditions. All five sites were analyzed for steady state conditions as a default, and soil properties were updated with additional experimental data. The basic analysis starts with a steady state model between 56.6 m³/s (2,000 cfs) and 565 m³/s (20,000 cfs),

and special cases such as overbank flow, rapid drawdown, and step down conditions are considered as additional analyses. If a riverbank is determined to be stable, then additional factors such as fluvial erosion, small scale failures, and soil property changes are considered in the analysis. The procedure for the slope stability analysis is outlined in Figure 5.1.

5.1 Fluvial Erosion

Fluvial erosion can be estimated with erodibility coefficient (k_d), critical shear stress (τ_c), and applied shear stress by the flow (τ_o). These parameters are determined using the jet erosion test and 3D computational fluid dynamics. In addition to these efforts, cumulative erosion pin data from 2005 to 2009 is available (Schenk et al. 2010). This data provides insight into the erosion rates found on the lower Roanoke River. Assuming that the soils at each site have similar values of the erodibility coefficient and critical shear stress, the amount of erosion can also be assumed to be proportional to the shear stress applied by the flow. Thus, the distribution of boundary shear stress is assumed to be same as the erosion profile during each period.

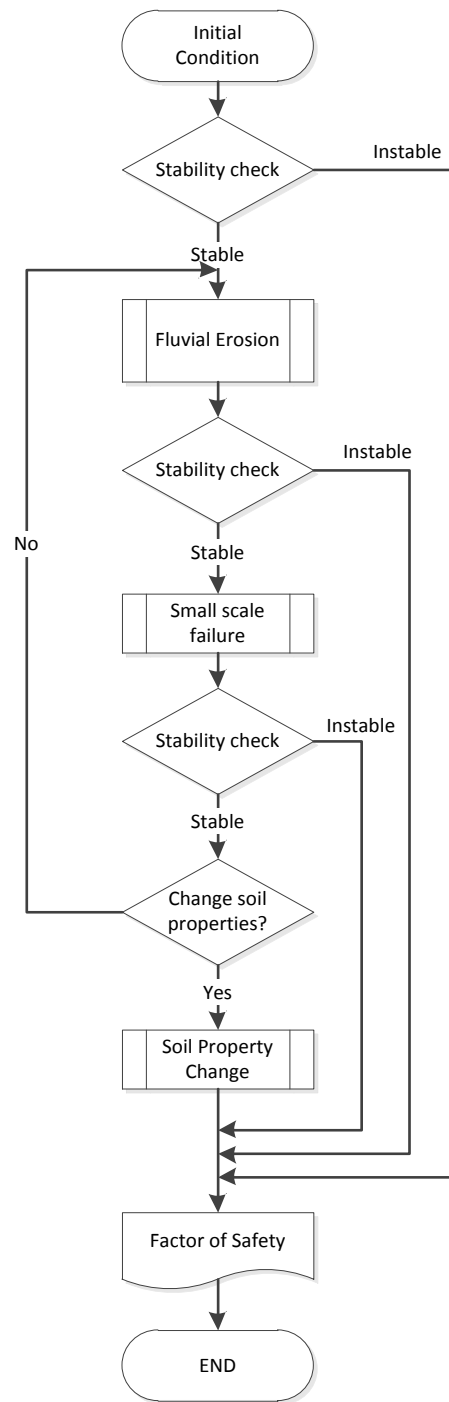
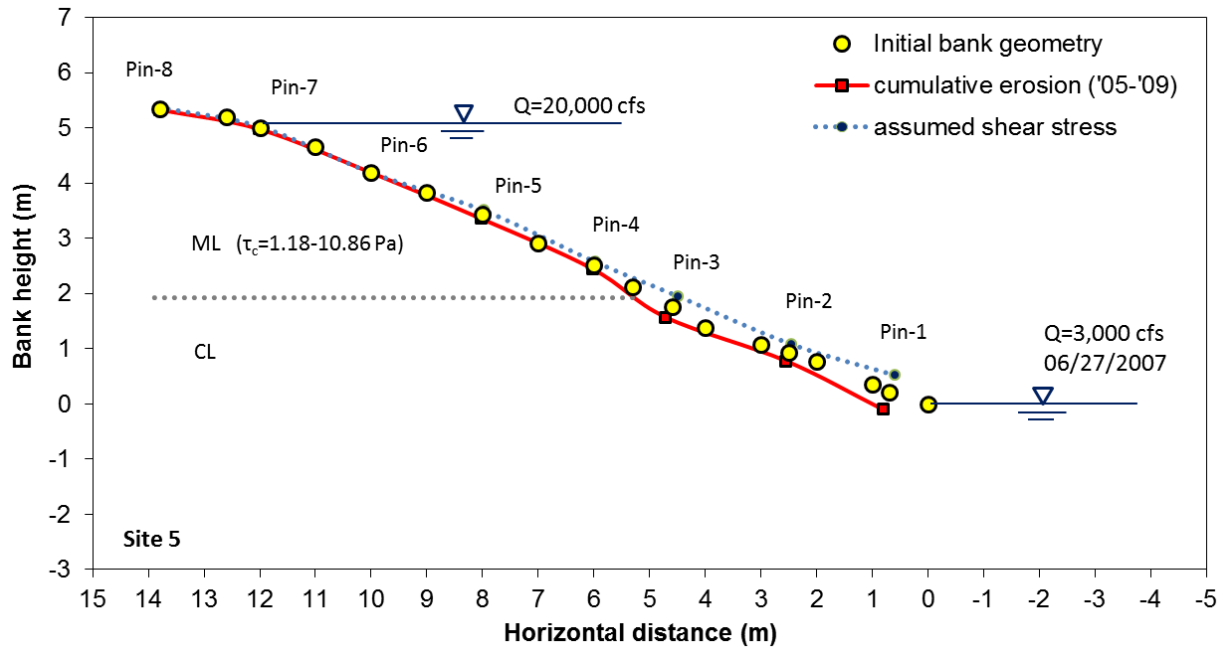
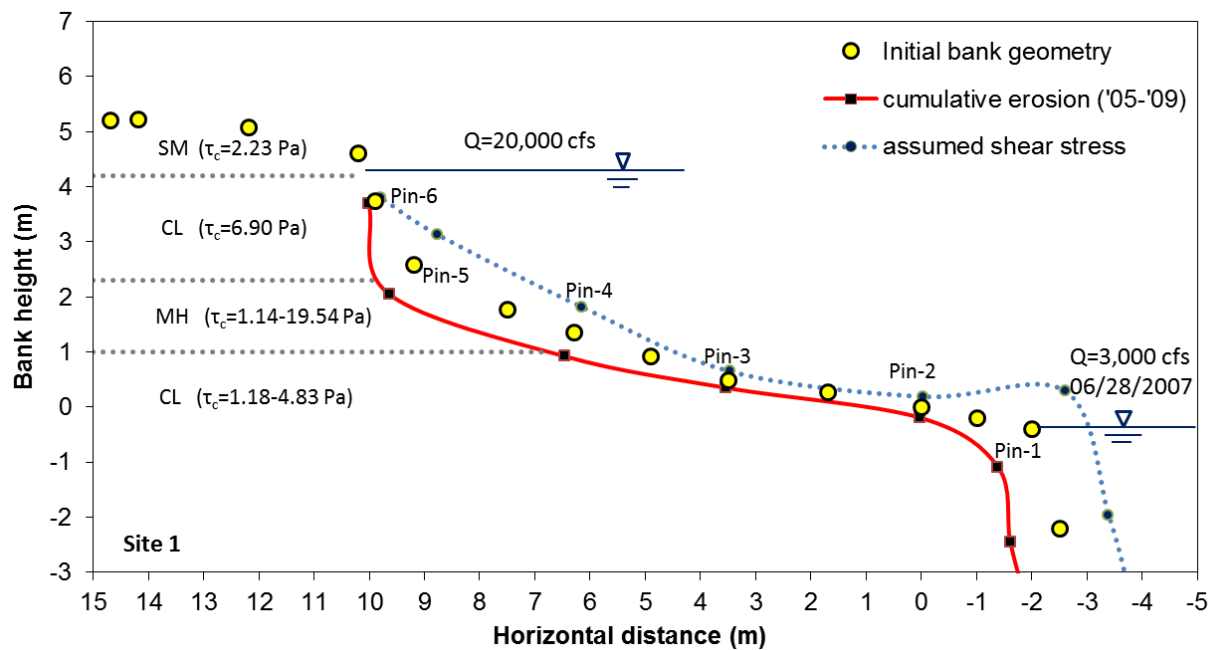


Figure 5.1. Flowchart illustrating the procedure for the slope stability analysis.

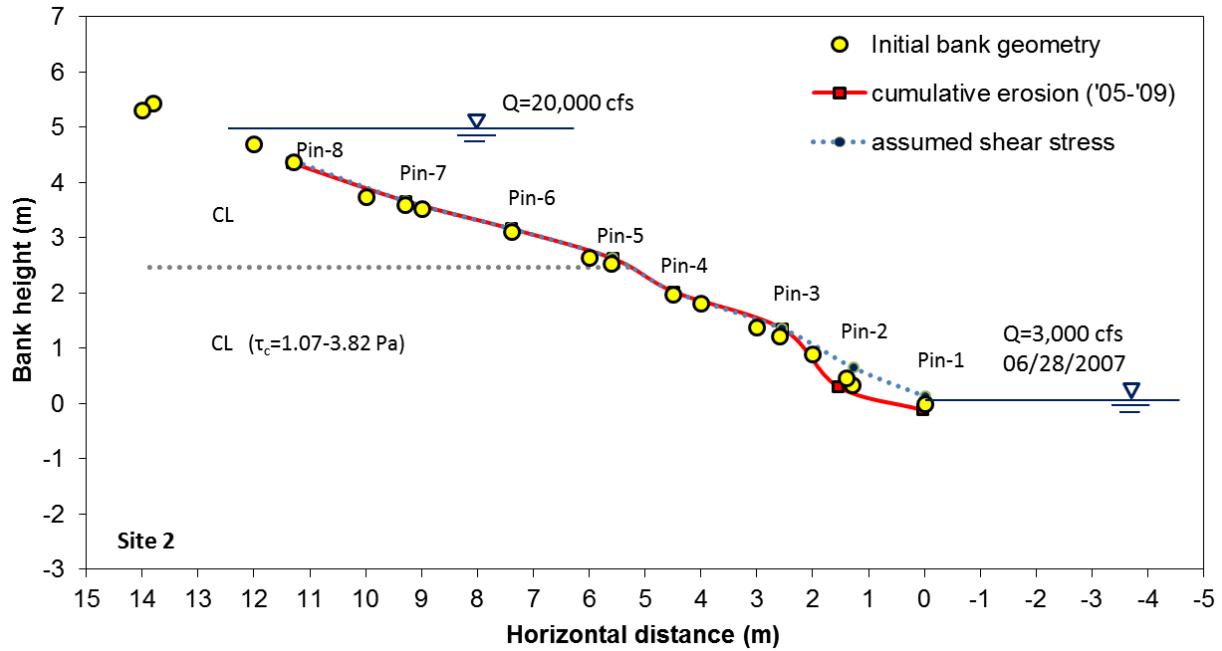


(a) Site 5 (straight channel)

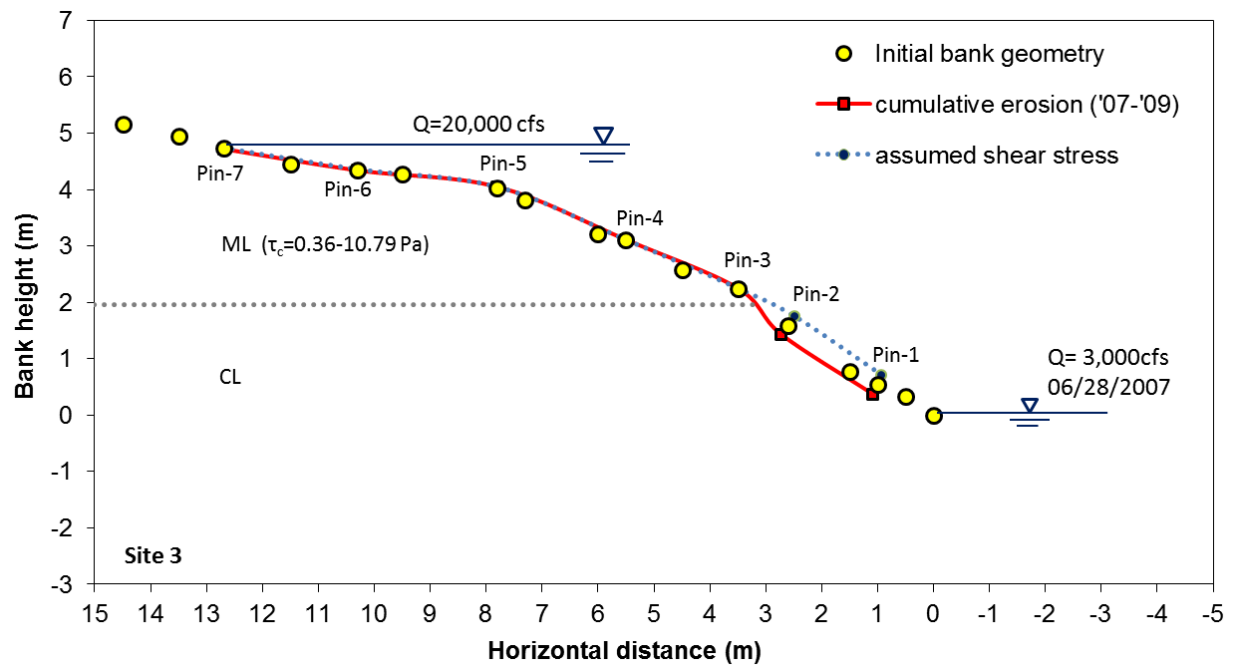


(b) Site 1 (outer bank)

Figure 5.2. Cumulative erosion based on the erosion pin data of Schenk et al. (2010) at different sites. Continued on the following page.



(c) Site 2 (straight channel)



(d) Site 3 (inner bank)

Figure 5.2. Cumulative erosion based on the erosion pin data of Schenk et al. (2010) at different sites.

5.2 Small Scale Failures

After extensive slope stability analysis, it was found that the riverbanks are stable under the steady state flow conditions investigated. However, a number of mass failures and lateral retreats have been observed in the study reach (Hupp et al. 2009; Petrie et al. 2009). It was then assumed that the riverbanks are initially stable as they exist in nature, but some of the banks become less stable due to the effects of destabilizing factors. When one factor is dominant or some factors accumulate to a critical point, the riverbank may fail.

The authors observed evidence of small scale failures in the field, which are an important bank retreat process and could contribute to larger instability of the bank. The small scale failures were as small as a half meter wide, and some of them were as large as 3 meters wide as shown in Figure 5.3. They were typically observed near the water surface when the discharge was low, making the depth of the failure difficult to identify. However, the observed locations and shapes indicate that the small scale failure could be the result of a combination of vertical cracks and fluvial erosion. The small scale failures may also trigger a large scale failure due to the loss of soils near toe of the bank slope.



Figure 5.3. Small scale failures on the lower Roanoke River.

Resistance to small scale failures was analyzed assuming a simple bilinear wedge failure near the water surface. In addition, the failure surface was developed within a predefined zone in the numerical models to check for small scale failures and the influence of tension cracks.

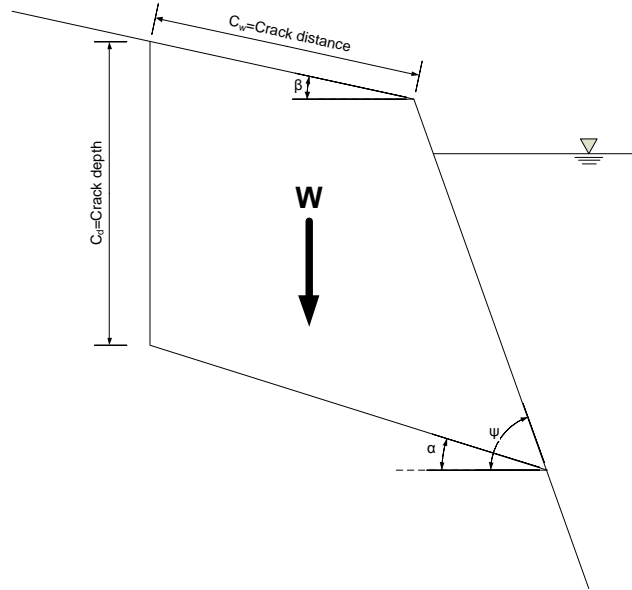


Figure 5.4. Schematic view of small scale failures.

The factor of safety for small scale failures is determined by calculating the driving and resisting forces on the soil mass, where the driving force is the gravity force parallel to the slip surface, and the resisting force is the sum of the forces normal to the slip surface and shear strength parameters.

$$FS = \frac{\text{Resisting Force}}{\text{Driving Force}} = \frac{F_R}{F_D}$$

$$F_R = c'l + N \tan \phi' \quad (5.2)$$

$$F_D = W \sin \alpha + U_{WTC} \cos \alpha - U_{SWE} \sin(\psi - \alpha)$$

Where U_{WTC} is the hydrostatic force applied by water within the crack, and U_{SWE} is hydrostatic force applied by the river water.

6. Overbank Flows

Based on field observations, a flow rate of $565 \text{ m}^3/\text{s}$ (20,000 cfs) produces bankfull conditions throughout the lower Roanoke River study reach. Once the flow rate is increased, river water will enter the floodplain, resulting in overbank flow. Overbank flow introduces considerable complexity due to a number of factors. The interaction of the flow in floodplain with that of the main channel can alter the flow and shear stress distribution from those for bankfull conditions (Shiono & Muto 1998). Figure 6.1 provides an overview of the changes in flow dynamics. Floodplains typically contain significantly more and varied vegetation than is seen in the main channel. This increase in vegetation has a strong effect on flow resistance and, thus, the roughness parameter. Additionally, Changes in soil type from the main channel to the floodplain can alter the roughness characteristics. Further discussion of overbank flows can be found in Knight & Shiono (1996) and Knight et al. (2010).

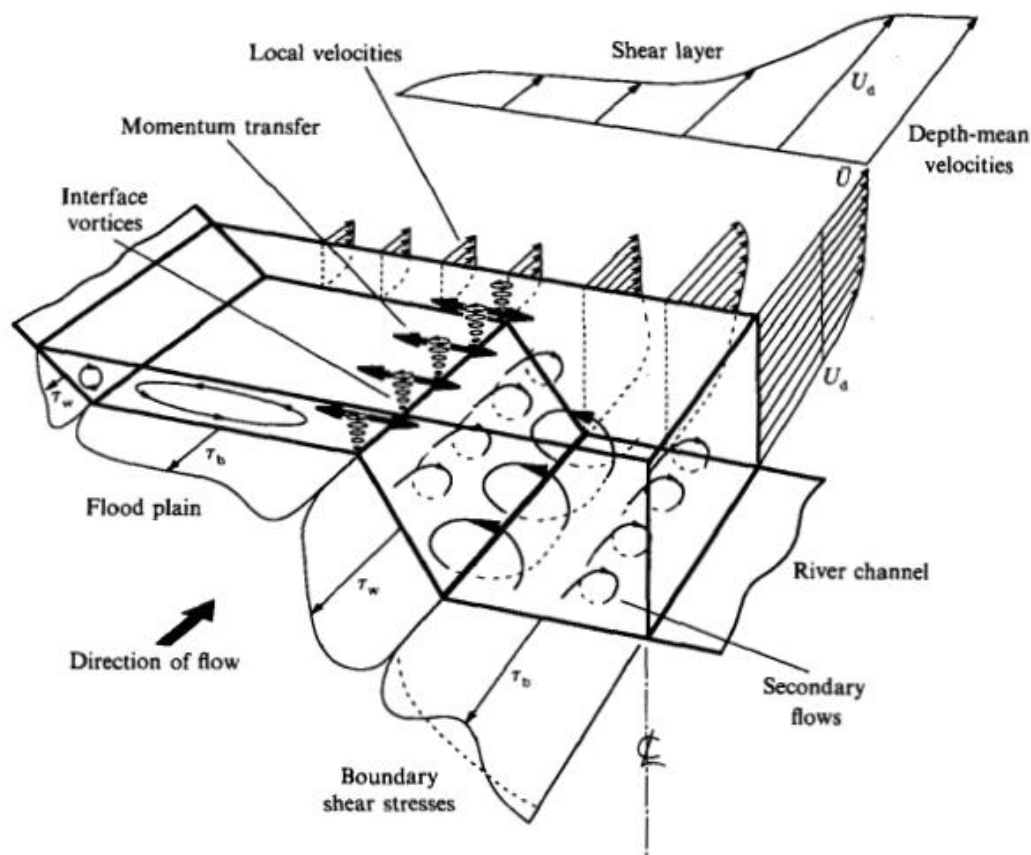


Figure 6.1. Summary of overbank hydraulics (Shiono & Knight 1991).

In terms of computational fluid dynamics (CFD) modeling, addressing floodplain vegetation represents a great challenge. Roughness due to the channel bed material can be characterized using a roughness parameter, such as the k_s -value used in this study. These grain roughness values are many times smaller than the flow dimensions. This is often not the case in the floodplain. Consider the simple case of overbank flow around a tree. The diameter of the tree is on the same order of magnitude as the local flow. The tree diameter may in fact, be larger than the flow depth. In this situation, modeling the roughness is no longer appropriate. Large-scale roughness elements, such as vegetation and floodplain structures, must be treated as part of the channel geometry. CFD modeling of flow through vegetation is only recently being investigated for carefully controlled laboratory flows (e.g. Stoesser et al. 2010a). Due to the complexity of addressing floodplain vegetation and the increased size of the computational domain, the authors are not aware of any study applying CFD to overbank flows in a natural river of comparable size to the lower Roanoke River. A detailed discussion of the effects of roughness on flow is provided by Raupach et al. (1991).

The effect of overbank flows on riverbank stability is primarily through changes in soil moisture and confining pressure. Prolonged overbank flows will result in fully saturated conditions within the riverbank, which acts to decrease stability. Also serving to destabilize the bank is the weight of the water flowing in the floodplain. These actions are countered by an increase in confining pressure due to the rise in water surface elevation. The critical condition for stability will likely occur after the water surface elevation has dropped but the bank remains fully saturated. The combination of excess pore pressure due to the saturated soil and the loss of confining pressure from the river water can result in mass failure. This situation is referred to as rapid drawdown (Duncan & Wright 2005).

The approach here will employ a simplified analysis to provide a rough estimate of the impact of a flow rate of $990 \text{ m}^3/\text{s}$ (35,000 cfs), which will likely result in overbank flows over much of the lower Roanoke River. The conclusions here are limited to the impact on erosion and riverbank stability and the impacts on hydraulic structures, such as bridges, as well as floodplain structures and habitat are not addressed. Due to previously discussed difficulties with CFD of overbank bank flows, the shear stress distribution for a discharge of $565 \text{ m}^3/\text{s}$ (20,000 cfs) is used. While

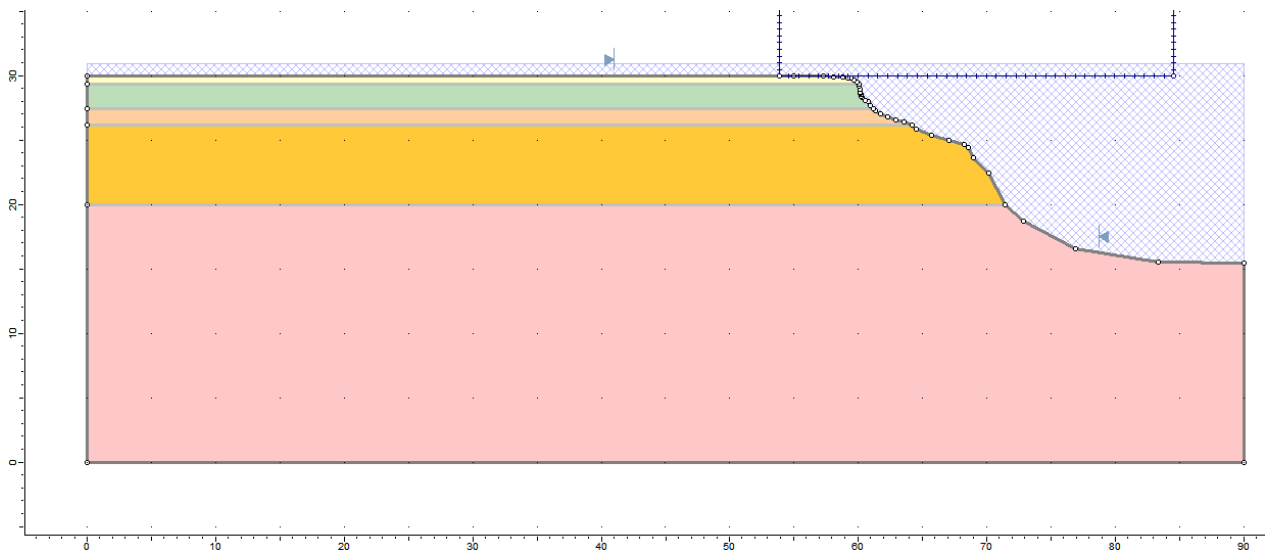
the applied shear stress will generally increase with an increasing flow rate, the change is difficult to estimate. Evidence exists that suggests that changes in flow patterns result in a small increase in applied shear stress once the flow enters the floodplain than if the flow is at bankfull condition. Given that it is unlikely that dramatic increase in shear stress will take place for the overbank flow conditions, the shear stress distribution for $565 \text{ m}^3/\text{s}$ (20,000 cfs) provides a useful estimate for this simplified analysis. Whether the flow is within the main channel or in the floodplain does not have a direct impact on the slope stability analysis so long as changes in the water surface elevation and soil moisture conditions are taken into account. Therefore, steady state and transient slope stability analyses are carried out following the same procedure as for within-bank flow as described in Petrie et al. (2009).

To determine the water surface elevation (WSE) at different discharge rates, data from HEC-RAS, USGS gage stations at Scotland Neck (SN) and Oak City (OC), NC, and local measurements at each site were combined and correlated to the bank geometries for numerical modeling. However, simulating overbank flow condition with HEC-RAS is not available due to the limited information on flood plain roughness. Thus, the water surface elevation for overbank flow is estimated using historical data from the USGS gage station.

A flow rate of approximately $963 \text{ m}^3/\text{s}$ (34,000 cfs) was measured from April 12 - May 1, 2003 (2440 hrs to 2890 hrs in 2003). Previous results considering a flow rate of $565 \text{ m}^3/\text{s}$ (20,000 cfs) indicated that the WSE at each site is similar to the average of USGS gage station heights at SN and OC. Although there is no historical data to support this correlation technique for overbank flow condition, it is assumed that same relationship is valid for overbank flow conditions. Thus, the height increase at Site 1 after $565 \text{ m}^3/\text{s}$ (20,000 cfs) to $990 \text{ m}^3/\text{s}$ (35,000 cfs) is determined as shown in Table 6-1. The height increase at the other sites is calibrated with the known relationships for other flow rates between Site 1 and the other sites.

Table 6.1. Water surface elevations during flood flow condition

Date	Duration (hr)	Flow rate (cfs)	Scotland Neck (m)	Oak City (m)	Average (SN+OC) (m)
1/6/2007 - 1/27/2007	516	20,000 cfs	7.58	6.22	6.90
4/13/2003 - 4/29/2003	394	34,000 cfs	9.08	6.63	7.86
Difference	N/A	14,000 cfs	1.5	0.41	0.96

**Figure 6.2.** Modeling of flood flow condition (Q=35,000 cfs).**Table 6.2.** Extended results of slope stability modeling (steady state)

Site 1	Discharge (cfs)						
	2,000	5,000	8,000	11,000	15,000	20,000	35,000
WSE* (m)	24.2	25.7	26.8	27.7	28.6	29.7	31.0

*Bank top elevation: 30m

Short term fluctuations in discharge from the dam, such as peaking operations, do not cause instant changes in the downstream WSE. However, if high flow conditions continue long enough to saturate the riverbanks, the step-down scenario may influence the riverbank stability. If the step-down durations are too short, the pore pressure in the bank may not dissipate, resulting in rapid drawdown. Thus, step-down rate needs to be determined and analyzed for slope stability.

(1) Rapid drawdown

When the WSE drops quickly where bank materials are impermeable or have low permeability, excess pore pressure develops in the soil while confining water pressure is removed. Thus, the riverbank may become unstable until the pore pressure is allowed to dissipate. Rapid drawdown may occur during a step-down scenario if the step-down period is too short and soil permeability is too low. As shown in Figure 6.3, flow data in January 2009 was considered as a rapid drawdown case, and all five sites were reviewed. The discharge was determined by several peaking events following an extended period of high flow. The downstream WSE did not appear to be affected by the peaking events.

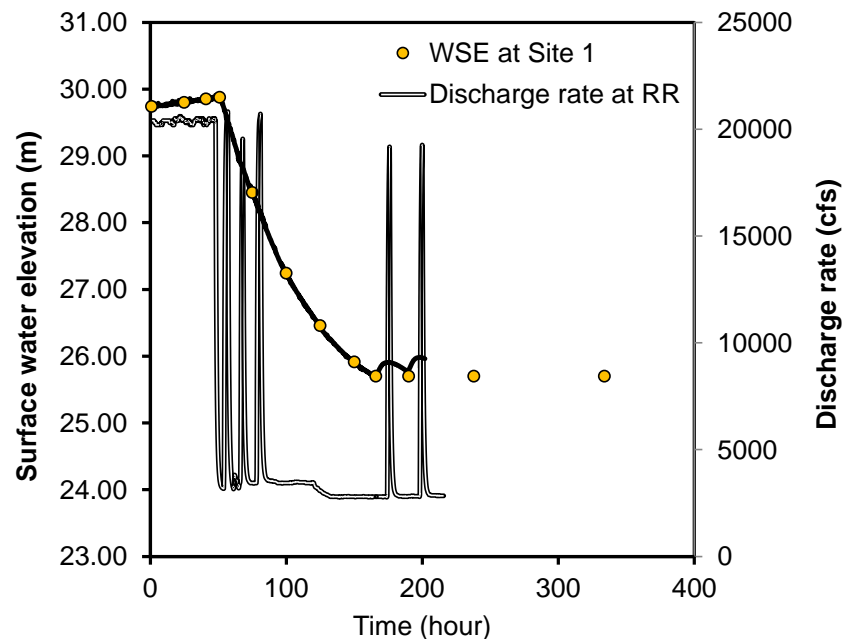


Figure 6.3. WSE changes at Site 1 as the result of several peaking events (January 2009).

(2) Step-down

A step-down flow scenario was selected from the USGS gage data in June 2009. Figure 6.4 shows a typical step-down operation dropping from 565 m³/s (20,000 cfs) to 56.6 m³/s (2,000 cfs) after 4 steps over a period of 17 days. Each step lasted about 100 hours or less. However, it is clear that the step-down does not cause an instant response in the water surface elevation, and it is regarded as a rapid drawdown case with a slow drawdown rate. Thus, it is expected that the step-down scenarios will be less critical than rapid drawdown due to the longer period which allows the excess pore pressure to dissipate.

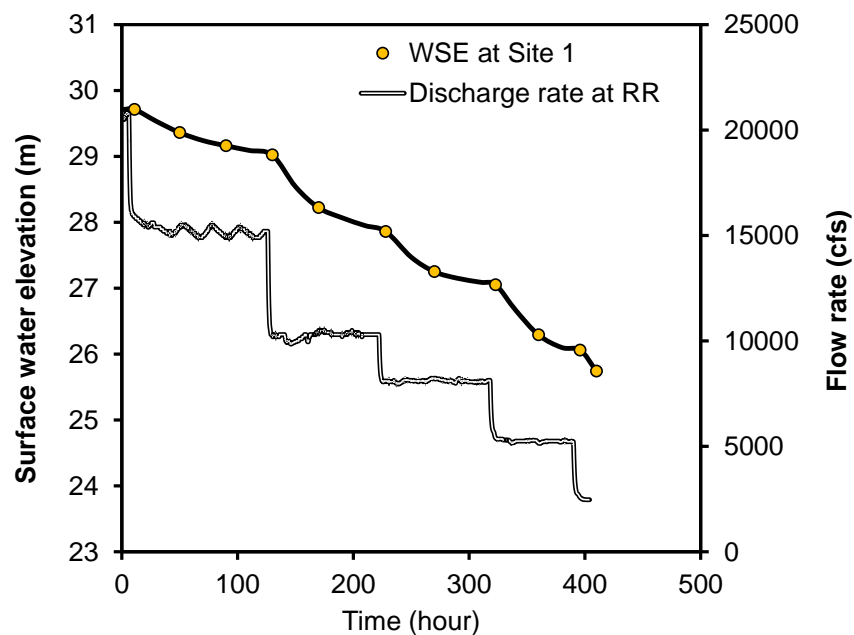


Figure 6.4. Step-down flow rate and WSE at Site 1 (June-July 2009).

7. Results

7.1 Fluvial Erosion

Fluvial erosion is calculated using the boundary shear stress distribution from the CFD simulations and the erodibility parameters, k_d and τ_c , determined from the jet test data. The erosion rate is then found using equation (2.1). The boundary shear stress values on the banks were found to be less than the mean critical shear stress value, indicating that erosion does not occur on average. However, some jet test data did predict lower values of critical shear stress. This finding suggests that there are locations on the bank that are more susceptible to erosion. The spatial distribution of the erodibility parameters is difficult to predict given the time intensive nature of the jet tests and limited access to the banks due to the river water. For this reason a single value for each parameter is taken to be representative of the entire bank.

A conservative approach was adopted to assess the impact of fluvial erosion. The dataset of erodibility parameters was reduced by selecting only the values for Site 1 below the median. These values are taken to be representative of the soils at the site which are more susceptible to erosion. The median values of the erodibility parameters were then found for the reduced dataset. The procedure resulted in the following values: $k_d = 4.55 \times 10^{-7} \text{ m}^3/\text{N}\cdot\text{s}$, $\tau_c = 2.95 \text{ Pa}$. Combining these erodibility parameters with equation (2.1), total amounts of erosion were predicted for period of one and five years. The duration of flows over $565 \text{ m}^3/\text{s}$ (20,000 cfs) was determined using the average exceedance value for the past four years. Figure 7.1 illustrates the resulting erosion. The applied shear stress by the flow was assumed to not change significantly due to changes in geometry due to erosion.

The maximum amount of erosion is 0.30 m (0.98 ft) for one year and 1.17 m (3.84 ft) for four years. It should be reiterated that these values are conservative and it is unlikely that similar erosion rates will occur over an entire riverbank. Even so, these calculated erosion values are not large enough to impact the bank stability. The minimum erosion calculated is zero for both time periods due to the fact that the applied shear stress on the upper portion of the bank did not exceed the critical shear stress. Schenk et al. (2010) measured a minimum erosion of 0.12 m (0.40 ft) and a maximum of 0.92 m (3.00 ft) at the same site after four years.

While the difference between the maximum predicted and measured values is about 20%, a direct comparison is not entirely appropriate. The erosion pins extend from the top of the bank to around the low flow water surface location. For this reason, the erosion pin data does not cover the entire riverbank. The numerical approach calculated the maximum erosion values near the bank toe. For much of the region covered by the erosion pins, no erosion was predicted in the numerical results. One possible explanation for this discrepancy is the process of “vertical zoning” (Couper 2003). “Vertical zoning” states that, for cohesive soils with high silt-clay content, different processes are dominant in generating erosion for different locations of the bank. Subaerial, or weathering, processes tend to dominate near the top of the bank while flow-induced shear stress primarily generates erosion at the bottom of the bank. The erosion pin data may then encompass the effects of subaerial processes, while the numerical results only represent the contribution of fluvial erosion.

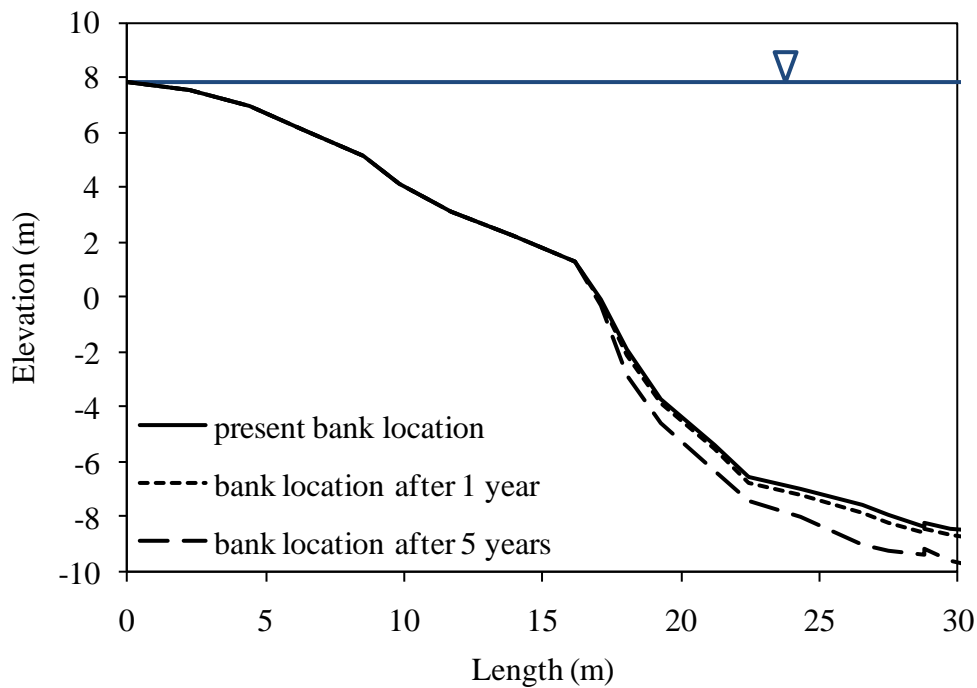


Figure 7.1 Estimated erosion of the left bank at Site 1. The water surface elevation for a flow rate of $565 \text{ m}^3/\text{s}$ (20,000 cfs) is shown.

7.2 Slope Stability

Slope stability at all five sites was analyzed for seven different steady state flow conditions, including one flow rate which will produce overbank flow (35,000 cfs). All slopes were found to be stable, and the previous findings were confirmed that the banks become more stable as the water surface elevation (WSE) rises. A few exceptional cases seem to be related to the shape of the failure envelope and effects of unsaturated shear strength.

Table 7.1. Factor of safety at each site for steady state flow conditions.

Flow rate (cfs) Site	2,000	5,000	8,000	11,000	15,000	20,000	35,000
S1	1.92	1.99	2.10	2.21	2.37	2.62	2.70
S2	1.84	1.81	1.82	1.85	1.91	1.94	2.29
S3	2.07	2.06	2.18	2.34	2.51	2.77	2.89
S4	1.74	1.70	1.63	1.65	1.63	1.77	2.05
S5	1.80	1.87	1.95	2.07	2.24	2.52	2.70

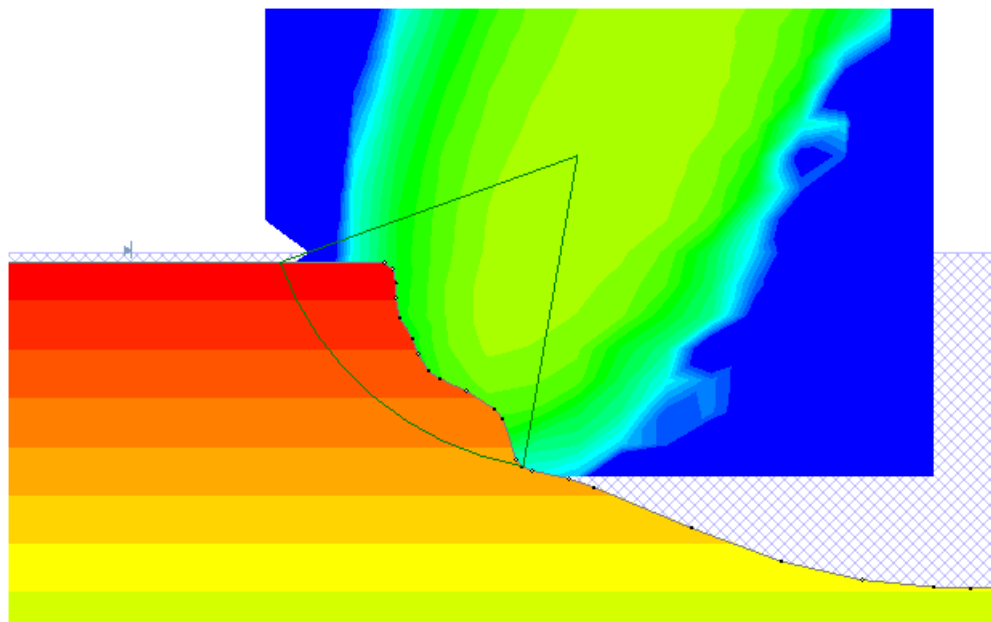


Figure 7.2. Example of overbank flow conditions at Site 4.

7.3 Small Scale Failures

Small scale failures were reviewed by adapting tension cracks to the slope stability analysis. When tension cracks develop, there is a loss of length in shear plane. Additionally, if the crack fills with water, the hydrostatic pressure exerted by the water acts as a driving force, which serves to decrease stability. Cracks may occur when tension develops in cohesive soils, and the maximum depth is generally estimated by adapting active earth pressure theory. Subaerial processes, such as desiccation, may contribute to cracking. Couper (2003) has demonstrated that cohesive soils with high silt-clay contents are especially susceptible to subaerial processes. Cracks can also develop as a result of a steep or overhanging soil mass created by undercutting fluvial erosion or desiccation of cohesive soils. However, numerical analysis of overhanging soil masses can be difficult.

Generally, a large failure line was predicted as the most critical envelope, and the tension cracks near the river did not affect the factor of safety as the crack did not meet the predicted envelop. However, when different depths and lengths of cracks were manually added and the failure line was forced to pass through the cracks as shown in Figure 7.3, the factor of safety decreased but the slope was still determined to be stable.

Small scale failure is difficult to predict with traditional slope stability analysis due to the numerical error caused by the relatively small denominator in the factor of safety equation, equation (5.2). When a riverbank consists of highly cohesive soils, there is an increased chance to have such an error.

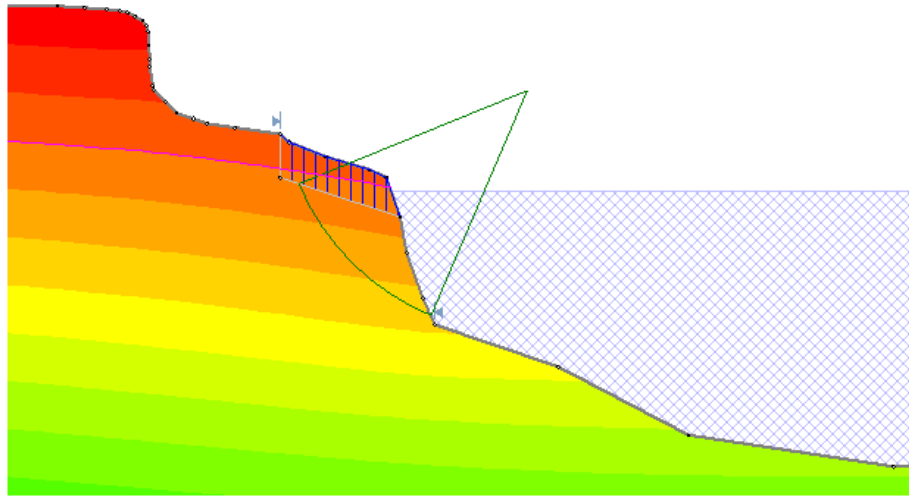


Figure 7.3. Example of a small scale failure with tension cracks near the WSE at Site 1.

7.4 Rapid Drawdown and Step-down Scenarios

Similar to the findings by Petrie et al. (2009), the riverbanks at all five study sites experienced a reduction in factor of safety during a drawdown event. Although it is known that rapid drawdown is a common critical condition for slope stability, all sites were found to remain stable for a conservative drawdown event, taken from the fastest drawdown rate that occurred between 2005 and 2009. The change in the factor of safety with decreasing WSE for all five sites is provided in Figure 7.4. While a decrease in factor of safety can be seen, the values remain above 1.0 for all sites, indicating a stable bank. This fact seems to be due to the high permeability values of the soil and the conservative drawdown rates.

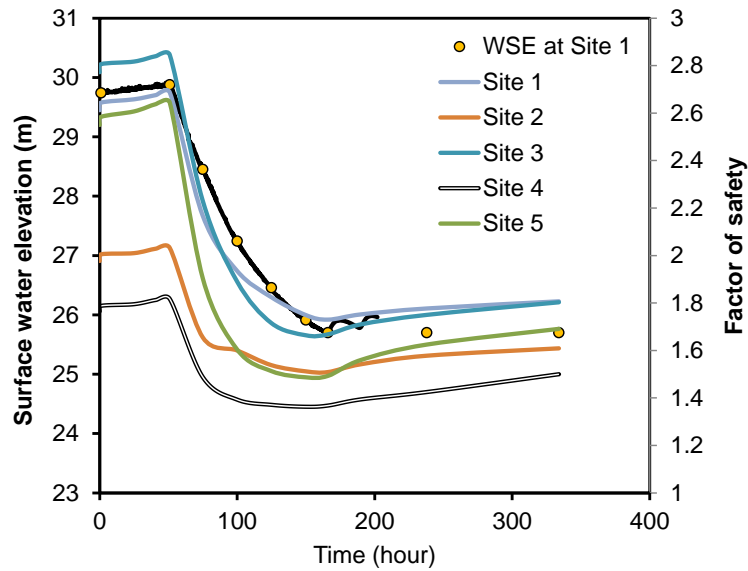


Figure 7.4. Changes in factor of safety over time during a rapid drawdown event.

As expected from the results of changes in WSE vs. time curves, Figures 6.3 and 6.4, the step-down scenario shows the exactly same trend that the factor of safety drops as the WSE decreases. Larger values of the permeability coefficient, which was also expected by ground water table observation, could be responsible for the nearly instant changes of factor of safety. The favorable drainage conditions in the riverbanks help to dissipate the excess pore pressure, and thus, the factor of safety seems to be directly related to the magnitude of confining pressure by river water. Additionally, the gradual decrease in WSE during the step-down scenario indicates that step-down is not as critical as rapid drawdown. Therefore, as long as the step-down rate does not cause a dramatic drop in the downstream WSE, the riverbanks will remain stable.

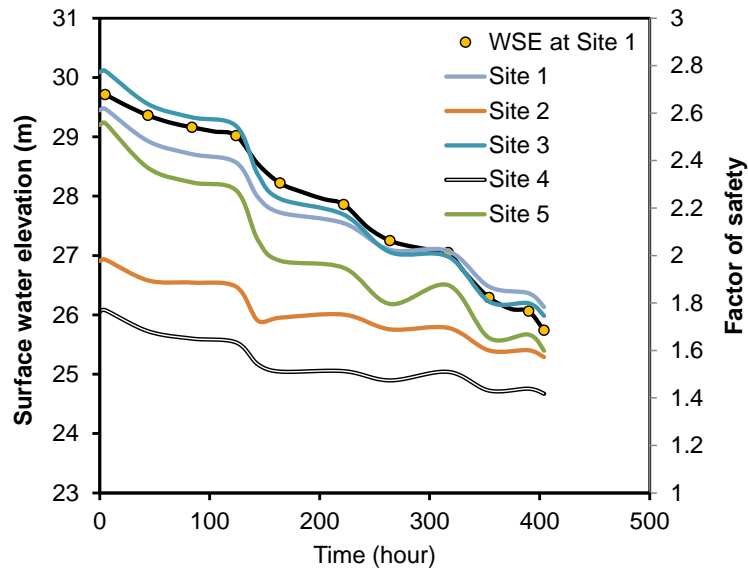


Figure 7.5. Factor of safety at each site for step-down flow conditions.

Decaying roots, earth worms and other soil-dwelling species, fissures, cracks, or structured soils could cause preferential flow which explains the unusually high in situ permeability. This also can explain not only the high values but also the wide range of in situ permeability.

Although the response of the groundwater table to WSE drawdown in the modeling results indicates that excess pore pressure dissipates quickly and in situ observation supports the results, the typical range of permeability values for those soil types in the field is closer to the results of the laboratory tests. As a conservative analysis, considering the worst case scenario due to the temporal and spatial heterogeneity of soils, both rapid drawdown and the step-down scenarios are evaluated using the lowest permeability values which are 10 to 500 times lower than those from the in situ tests.

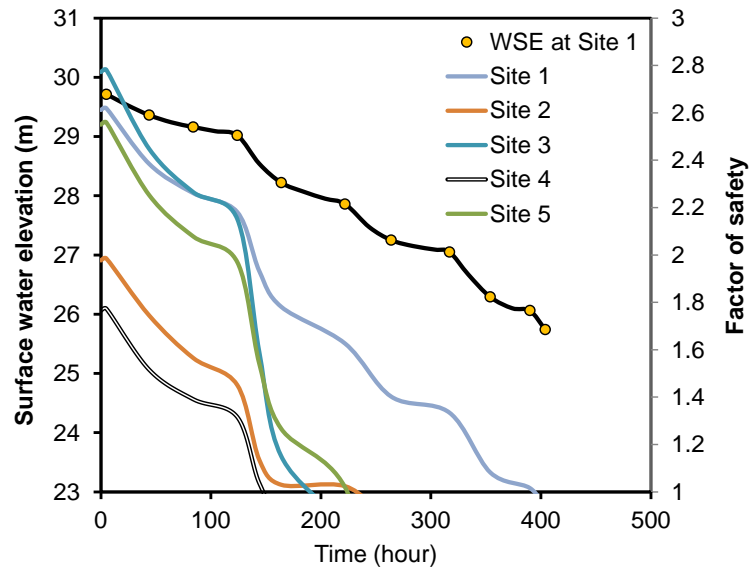


Figure 7.6 Factor of safety with lower permeability for step-down flow scenario.

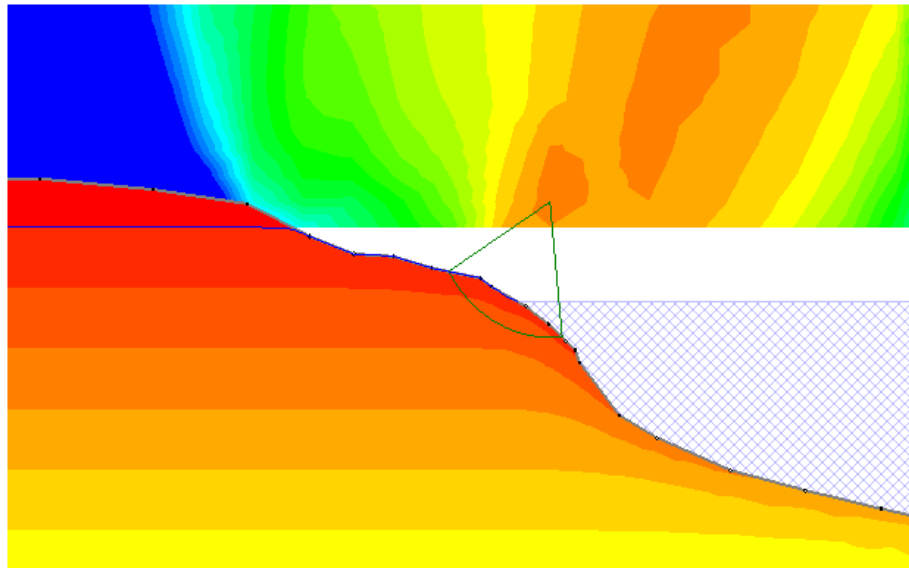


Figure 7.7. Unstable slope after step-down with lower permeability.

Both rapid drawdown and step-down scenarios using the lowest permeability values result in less stable conditions. However, some of the calculated factors of safety may contain numerical errors resulting in rapid drops in the factor of safety after 124 hours, as shown in Figure 7.6. These errors occur when the calculated effective normal stress is negative (Rocscience Inc. 2010). High pore pressure, steep geometry, and tensile stress in the soils can generate the error in

the slope stability program. Despite the presence of some numerical error, it can still be concluded that higher excess pore pressure is responsible for the less stable banks. In addition, the shape of the failure line appears small and shallow, as shown in Figure 7.7, which could help explain the occasional small scale local failures observed in the field. Thus, the excess pore pressure could be one of the driving factors in small scale failures.

7.5 Coupled Stability Analysis

Riverbank stability analysis is typically determined by a given bank geometry and soil properties. However, in reality, those conditions continuously change due to the dynamic environment in the river. The change in flow rate due to reservoir releases on the lower Roanoke river serves as one example. While the slope stability analysis predicted the study sites to be stable for all conditions, fluvial erosion can also influence stability. A common example is when fluvial erosion occurs near the bank toe which results in a steeper slope thereby decreasing stability.

In addition to the complex interparticle forces present in cohesive soils, natural temporal and spatial variability at a site further complicate attempts to quantify erosion. The jet test results provide evidence of the range of spatial variability that can be seen at a single site within similar soil types. The erosion pin data from Schenk et al. (2010) covers several years and provides a useful tool. Using the average erosion rate at each site, fluvial erosion for next ten years is predicted as shown in Figures 7.8 and 7.9. This analysis assumes that the future flows are similar, in terms of the duration of high flows, to the flow from the previous five years (2005-2009), the period over which the erosion pin data was collected.

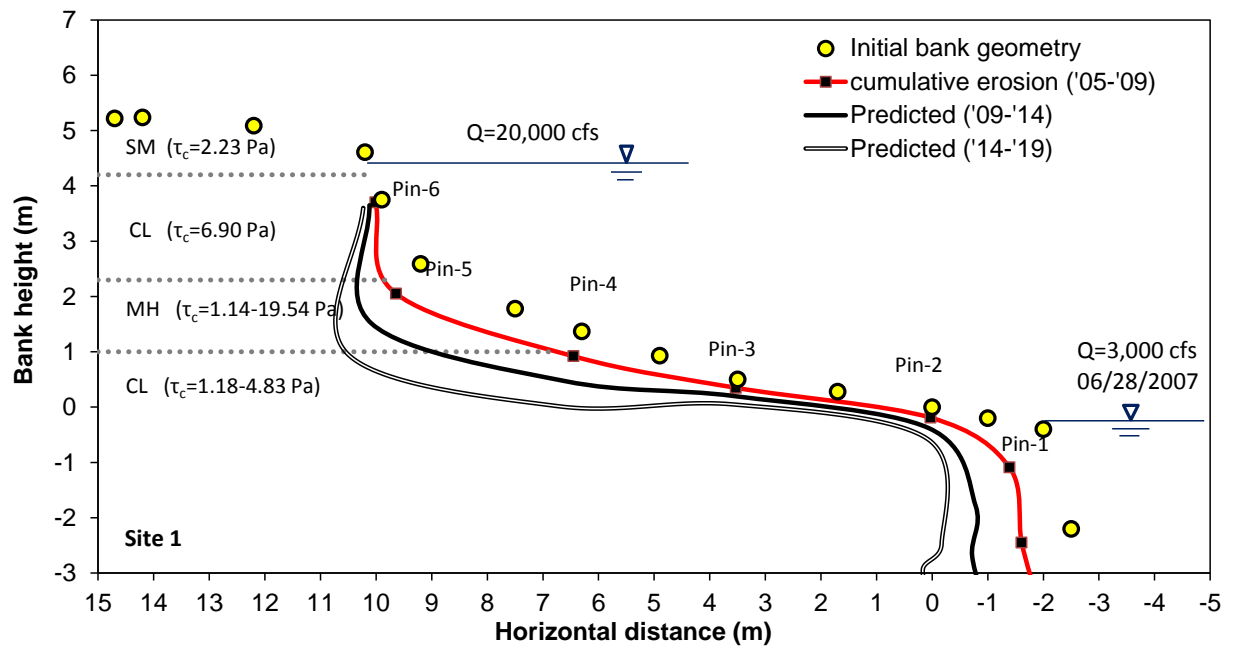


Figure 7.8. Prediction of profile changes due to fluvial erosion over ten years at Site 1.

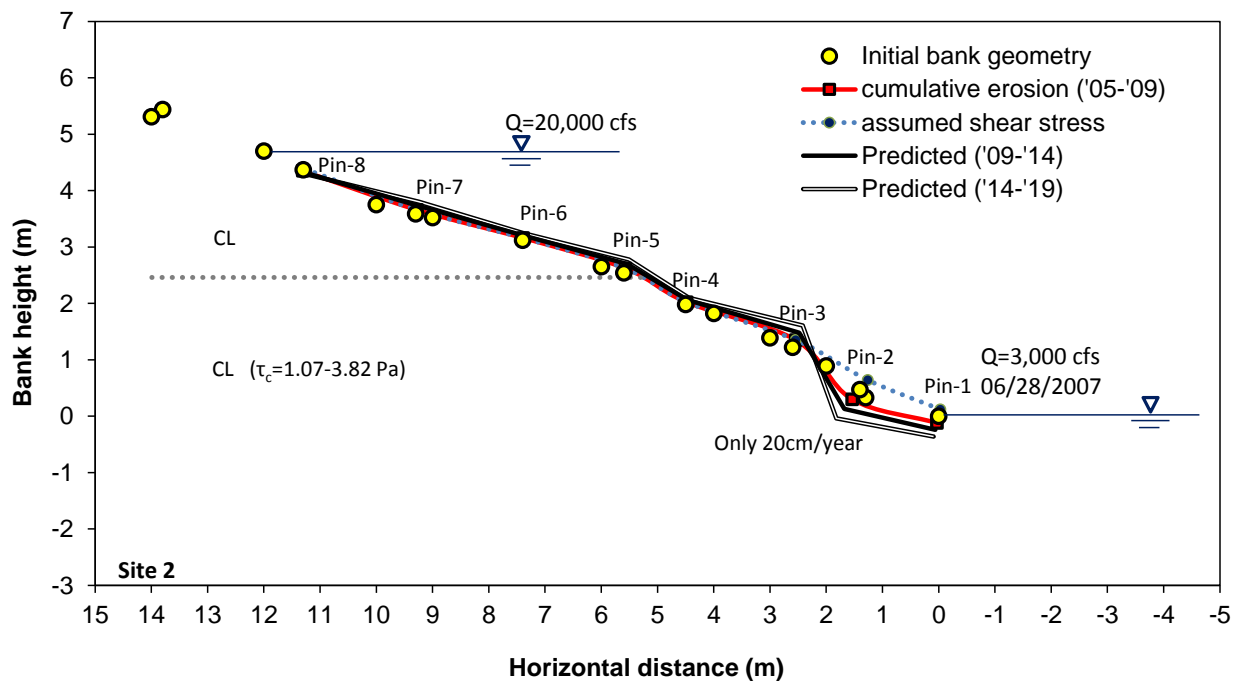


Figure 7.9. Prediction of profile changes due to fluvial erosion over ten years at Site 2.

Using the cumulative erosion data from 2005 to 2009, fluvial erosion for next ten years is estimated as shown in Figure 7.8 and 7.9, and then the factor of safety is calculated. The bank geometry at each site was modified based on the erosion pin data, and analyzed under a flow of $56.6 \text{ m}^3/\text{s}$ (2,000 cfs). This flow rate produces the lowest factor of safety due to the loss of confining pressure as the water surface elevation decreases.

Table 7.2. Factor of safety changes after ten years of erosion estimated by USGS erosion pin data.

	Current		After 10 years	
	Max. Erosion (2004 – 2009)	FS at 2000 cfs	Cumulative erosion (m)	FS at 2000 cfs
Site 1	0.92	1.92	2.3	1.58
Site 2	0.22	1.84	0.55	1.83
Site 3	0.2*	2.07	1.0	1.83
Site 4	N/A	1.74	0.80 (assumed)	1.61
Site 5	0.33	1.80	0.83	1.81

* 2007-2009

Site 1 and Site 4 are expected to be the least stable sites, which agrees with field assessments of the site conditions. The factor of safety slightly increased at Site 5 even with 0.80 m of erosion. This surprising result indicates that fluvial erosion can also occasionally improve bank stability.

8. Conclusions

The conclusions for this study are summarized and discussed below.

1. Fluvial Erosion

While laboratory tests for soil properties indicate that the different cohesive bank soil types are similar, a wide range of erodibility parameters were measured in situ with the jet test. This finding is supported by numerous previous studies that demonstrate the temporal and spatial variability of erodibility as well as the erosion pin data of Schenk et al. (2010). Generally, the cohesive riverbank soil are resistant to fluvial erosion and significant erosion is not expected for flows below $565 \text{ m}^3/\text{s}$ (20,000 cfs). However, lower critical shear stress values were found for several tests, indicating that some areas of the bank may be susceptible to fluvial erosion.

2. Soil Permeability

Soil permeability values measured in situ and in the laboratory differed by several orders of magnitude. The results from the in situ tests best matched the observations from the groundwater table monitoring. However, a conservative analysis using lower permeability is also considered for rapid drawdown and step down modeling.

3. Slope Stability

The riverbanks at the study sites are stable in their present condition with regards to large scale failures. However, small scale failures produce lower factors of safety especially in the presence of tension cracks. During the May 2010 field visit, cracks in the bank soil were observed and documented. Additionally, the riverbanks under rapid drawdown and step-down scenarios were also checked using the lowest permeability values, representing the most conservative calculation. The banks were determined to be less stable than with the higher permeability values due to the higher excess pore pressure. The vast majority of the riverbank length consists of soils with higher permeability values which render the banks stable. However, areas of low permeability soil may exist which likely explains the occasional small scale bank failures observed along the study reach.

4. Step-down Scenario

The step-down scenario described in the lower Roanoke River Betterment Plan does not have a negative effect on riverbank stability. The amount of time at each discharge is sufficient to allow the pore pressure to dissipate. While the factor of safety will decrease during step-down releases, the banks were found to remain stable. However, considering the heterogeneity and uncertainty of the soil characteristics represented by a wide range of permeability and jet test results, a shorter step-down period will decrease the riverbank stability, in general.

5. Increase in Flood Control Flow Rate

A flow rate of 35,000 cfs will result in overbank flow throughout much of the lower Roanoke River. Due to the increase in confining pressure, it was determined that the banks will remain stable. The numerical approach employs a simplified one-dimensional hydraulic model and is not able to determine the effects of the designated overbank flow on fluvial erosion. To properly account for erosion in overbank flows is a very challenging problem requiring more advanced and elaborate numerical simulations of fluid flow along with more detailed information about floodplain topography and roughness. Such a modeling effort could be the subject of a separate project.

9. References

- Annandale, G. W. (2006). *Scour technology: mechanics and engineering practice*, McGraw-Hill, New York.
- Akahori, R., Schmeeckle, M. W., Topping, D. J., and Melis, T. S. (2008). "Erosion properties of cohesive sediments in the Colorado River in Rand Canyon." *River Research and Applications*, 24(8), 1160-1174.
- Arulanandan, K., Gillogley, E., and Tully, R. (1980). "Development of a quantitative method to predict critical shear stress and rate of erosion of natural undisturbed cohesive soils." *Technical Report - US Army Engineer Waterways Experiment Station (GL-80-5)*, 99.
- ASTM D 2435 (2004). "Standard test methods for one-dimensional consolidation properties of soils using incremental loading." *ASTM International*.
- Bagarello, V., Iovino, M., and Reynolds, W. D. (1999). "Measuring hydraulic conductivity in a cracking clay soil using the Guelph permeameter." *Transactions of the ASAE*, 42(4), 957-964.
- Bates, P. D., Lane, S. N., and Ferguson, R. I. (2005). *Computational fluid dynamics: applications in environmental hydraulics*, J. Wiley, Chichester.
- Beltaos, S., and Rajaratnam, N. (1974). "Impinging circular turbulent jets." *Journal of the Hydraulics Division-Asce*, HY10, 1313-1328.
- Blaisdell, F. W., Anderson, C. L., and Hebaus, G. G. (1981). "Ultimate dimensions of local scour." *American Society of Civil Engineers Proceedings, Journal of the Hydraulics Division*, 107(3), 327-337.
- Boumans, J. H. (1953). "Het bepalen van de drainafstand met behulp van de Boorgaten methode." *Landbouwtijdschrift*, 82-104.
- Briaud, J. L., Ting, F. C. K., Chen, H. C., Cao, Y., Han, S. W., and Kwak, K. W. (2001). "Erosion function apparatus for scour rate predictions." *Journal of Geotechnical and Geoenvironmental Engineering*, 127(2), 105-113.
- Charonko, C. M. (2010). "Evaluation of an in situ measurement technique for streambank critical shear stress and soil erodibility." Blacksburg, Va: University Libraries, Virginia Polytechnic Institute and State University. <http://scholar.lib.vt.edu/theses/available/etd-06032010-142638/>.

- Chaudhry, M. H. (2008). *Open-channel flow*, 2nd Ed., Springer, New York.
- Clark, L. A., and Wynn, T. M. (2007). "Methods for determining streambank critical shear stress and soil erodibility: Implications for erosion rate predictions." *Transactions of the ASABE*, 50(1), 95-106.
- Couper, P. (2003). "Effects of silt-clay content on the susceptibility of river banks to subaerial erosion." *Geomorphology*, 56(1-2), 95-108.
- Darby, S. E., Rinaldi, M., and Dapporto, S. (2007). "Coupled simulations of fluvial erosion and mass wasting for cohesive river banks." *Journal of Geophysical Research-Earth Surface*, 112, F03022, doi10.1029/2006JF000722.
- Dawson, E. M., Roth, W. H., and Drescher, A. (1999). "Slope stability analysis by strength reduction." *Geotechnique*, 49(6), 835-840.
- Duncan, J. M., and Wright, S. G. (2005). *Soil strength and slope stability*, John Wiley & Sons, Hoboken, N.J.
- Ernst, L. F. (1950). "A new formula for the calculation of the permeability factor with the auger hole method." Agricultural Experiment Station T.N.O., Groningen, The Netherlands.
- Ferziger, J. H., and Perić, M. (2002). *Computational methods for fluid dynamics*, 3rd, rev. Ed., Springer, Berlin; New York.
- Fitzgerald, D. F., Price, J. S., and Gibson, J. J. (2003). "Hillslope-swamp interactions and flow pathways in a hypermaritime rainforest, British Columbia." *Hydrological Processes*, 17(15), 3005-3022.
- Hanson, G.J. and Cook, K.R. (1997). *Development of Excess Shear Stress Parameters for Circular Jet Testing*. ASAE Paper No. 97-2227, American Society of Agricultural Engineers, St. Joseph, Michigan.
- Hanson, G. J., and Cook, K. R. (2004). "Apparatus, test procedures, and analytical methods to measure soil erodibility in situ." *Applied Engineering in Agriculture*, 20(4), 455-462.
- Hanson, G. J., and Simon, A. (2001). "Erodibility of cohesive streambeds in the loess area of the midwestern USA." *Hydrological Processes*, 15(1), 23-38.
- Harvey, J. W., and Nuttle, W. K. (1995). "Fluxes of water and solute in a coastal wetland sediment. 2. Effect of macropores on solute exchange with surface water." *Journal of Hydrology*, 164(1-4), 109-125.

- Hodkinson, A. (1996). "Computational fluid dynamics as a tool for investigating separated flow in river bends." *Earth Surface Processes and Landforms*, 21(11), 993-1000.
- Hupp, C. R., Schenk, E. R., Richter, J. M., Peet, R. K., and Townsend, P. A. (2009). "Bank erosion along the dam-regulated lower Roanoke River, North Carolina." In: *Management and Restoration of Fluvial Systems with Broad Historical Changes and Human Impacts*, L. A. James, S. L. Rathburn, and G. R. Whittecar, eds., 97-108.
- Julian, J. P., and Torres, R. (2006). "Hydraulic erosion of cohesive riverbanks." *Geomorphology*, 76(1-2), 193-206.
- Knight, D. W., McGahey, C., Lamb, R., and Samuels, P. G. (2010). *Practical channel hydraulics: roughness, conveyance and afflux*, CRC Press, Boca Raton, Florida.
- Knight, D. W., and Shiono, K. (1996). "River channel and floodplain hydraulics." In: *Floodplain Processes*, M. G. Anderson, D. E. Wall, and P. D. Bates, eds., John Wiley & Sons, 139-181.
- Lane, S. N., Bradbrook, K. F., Richards, K. S., Biron, P. A., and Roy, A. G. (1999). "The application of computational fluid dynamics to natural river channels: three-dimensional versus two-dimensional approaches." *Geomorphology*, 29(1-2), 1-20.
- Marques de Sá, J.P. (2003). *Applied Statistics using SPSS, STATISTICA and MATLAB*, Springer, Berlin.
- Nam, S., Petrie, J., Diplas, P., and Gutierrez, M. S. (2010). "Effects of spatial variability on the estimation of erosion rates for cohesive riverbanks." *River Flow 2010, International Conference on Fluvial Hydraulics*, Braunschweig, Germany, 1309-1314.
- Newman, A. E. (2010). "Water and Solute Transport in the Shallow Subsurface of a Riverine Wetland Natural Levee." Master of Science, Baton Rouge.
- Patankar, S. V. (1980). *Numerical heat transfer and fluid flow*, Hemisphere Pub. Corp. McGraw-Hill, New York.
- Petrie, J., Nam, S., Diplas, P., and Gutierrez, M. (2009). "Effects of Within-Day and Within-Week Peaking on Bank Erosion at the Roanoke River Downstream of the Roanoke Rapids Dam." Report to Dominion and United States Army Corps of Engineers.
- Raupach, M. R., Antonia, R. A., and Rajagopalan, S. (1991). "Rough-wall turbulent boundary layers." *Applied Mechanics Reviews*, 44(1), 1-25.

Rocscience Inc. (2010). "SLIDE v6.0 Online Help."

<<http://www.rocscience.com/downloads/slide/webhelp/Slide.htm>>

Rüther, N., Jacobsen, J., Olsen, N. R. B., and Vatne, G. (2010). "Prediction of the three-dimensional flow field and bed shear stresses in a regulated river in mid-Norway."

Hydrology Research, 41(2), 145-152.

Schenk, E.R., Hupp, C.R., Richter, J.M., and Kroes, D.E. (2010). Bank erosion, mass wasting, water clarity, bathymetry, and a sediment budget along the dam-regulated lower Roanoke River, North Carolina: U.S. Geological Survey Open-File Report 2009–1260, 112 p., available online at <http://pubs.usgs.gov/of/2009/1260/>.

Shen, Y. and Diplas, P., 2010. Modeling Unsteady Flow Characteristics of Hydropeaking Operations and their Implications on Fish Habitat. *Journal of Hydraulic Engineering*, 136(12):1053-1066.

Shen, Y. and Diplas, P., 2008. Application of two- and three-dimensional computational fluid dynamics models to complex ecological stream flows." *Journal of Hydrology*, 348(1-2): 195-214.

Shiono, K., and Knight, D. W. (1991). "Turbulent open-channel flows with variable depth across the channel." *Journal of Fluid Mechanics*, 222, 617-646.

Shiono, K., and Muto, Y. (1998). "Complex flow mechanisms in compound meandering channels with overbank flow." *Journal of Fluid Mechanics*, 376(-1), 221-261.

Soilmoisture Equipment Corp. (2006). "2800K1 Guelph permeameter operating instructions."

Stoesser, T., Kim, S. J., and Diplas, P. (2010). "Turbulent Flow through Idealized Emergent Vegetation." *Journal of Hydraulic Engineering*, 136(12), 1003-1017.

Stoesser, T., Rüther, N., and Olsen, N. R. B. (2010). "Calculation of primary and secondary flow and boundary shear stresses in a meandering channel." *Advances in Water Resources*, 33(2), 158-170.

Strom, K. B., Papanicolaou, A. N., and Constantinescu, G. (2007). "Flow heterogeneity over 3D cluster microform: Laboratory and numerical investigation." *Journal of Hydraulic Engineering*, 133(3), 273-287.

Thoman, R. W., and Niezgoda, S. L. (2008). "Determining Erodibility, Critical Shear Stress, and Allowable Discharge Estimates for Cohesive Channels: Case Study in the Powder River Basin of Wyoming." *Journal of Hydraulic Engineering*, 134(12), 1677-1687.

- Tu, J., Yeoh, G. H., and Liu, C. (2008). *Computational fluid dynamics: a practical approach*, Butterworth-Heinemann; Boston.
- van Beers, W. F. J. (1983). *The auger hole method: A field measurement of the hydraulic conductivity of soil below the water table*, International Institute for Land Reclamation and Improvement, Wageningen, the Netherlands.
- Wilcox, D. C. (2006). *Turbulence modeling for CFD*, 3rd Ed., DCW Industries, La C nada, CA.
- Wynn, T. M. (2004). *The effects of vegetation on stream bank erosion*. Blacksburg, Va: University Libraries, Virginia Polytechnic Institute and State University.
<http://scholar.lib.vt.edu/theses/available/etd-05282004-115640/>.
- Wynn, T. M., Henderson, M. B., and Vaughan, D. H. (2008). "Changes in streambank erodibility and critical shear stress due to subaerial processes along a headwater stream, southwestern Virginia, USA." *Geomorphology*, 97(3-4), 260-273.
- Yakhot, V., and Orszag, S. A. (1986). "Renormalization group analysis of turbulence. I. Basic theory." *Journal of Scientific Computing*, 1(1), 3-51.

10. Appendices

Any of the following appendices can be added on request:

1. Bank and channel geometry for the study sites
2. Numerical mesh independence study for CFD models
3. In situ and laboratory permeability test results
4. Slope stability modeling of all study sites including input parameters